

# Digital Twin-Based Cooling System Optimization for Data Center

Shrenik Amol Jadhav <sup>a</sup>  and Zheng Liu <sup>b</sup> 

<sup>a</sup> Department of Computer and Information Science,  
University of Michigan-Dearborn, Dearborn, USA

<sup>b</sup> Department of Industrial and Manufacturing Systems Engineering,  
University of Michigan-Dearborn, Dearborn, USA

## Abstract

Data center cooling systems consume significant auxiliary energy, yet optimization studies rarely quantify the gap between theoretically optimal and operationally deployable control strategies. This paper develops a digital twin of the liquid cooling infrastructure at the Frontier exascale supercomputer, in which a hot-temperature water system comprises three parallel subloops, each serving dedicated coolant distribution unit clusters through plate heat exchangers and variable-speed pumps. The surrogate model is built based on Modelica and validated through one full calendar year of 10-minute operational data following ASHRAE Guideline. The model achieves a subloop coefficient of variation of the root mean square error below 2.7% and a normalized mean bias error within  $\pm 2.5\%$ . Using this validated surrogate model, a layered optimization framework evaluates three progressively constrained strategies: an analytical flow-only optimization achieves 20.4% total energy saving, unconstrained joint optimization of flow rate and supply temperature demonstrates 30.1% total energy saving, and ramp-constrained optimization of flow rate and supply temperature, enforcing actuator rate limits, can reach total energy saving of 27.8%. The analysis reveals that the baseline system operates at 2.9 times the minimum thermally safe flow rate, and the co-optimizing supply temperature with flow rate nearly doubles the savings achievable by flow reduction alone.

*Keywords:* Cooling system optimization; data center; digital twin; supercomputer; energy efficiency

## 1 Introduction

Global data center electricity consumption reached 415 TWh in 2024, approximately 1.5% of worldwide electricity demand, and is projected to exceed 945 TWh by 2030 ([International Energy Agency, 2025](#)). In the United States alone, data centers consumed 176 TWh in 2023 (4.4% of national electricity), with projections ranging from 325 to 580 TWh by 2028 ([Shehabi et al., 2024](#)). While advances in server efficiency and virtualization have

partially offset demand growth (Masanet et al., 2020), the proliferation of artificial intelligence workloads and the push toward exascale computing are placing unprecedented strain on cooling infrastructure. Cooling systems account for 30–40% of total data center electricity consumption (Zhang et al., 2021; Ebrahimi et al., 2014), making them the single largest controllable load in most facilities. Yet the global average Power Usage Effectiveness (PUE) has stagnated between 1.55 and 1.59 since 2020 (Uptime Institute, 2024), suggesting that incremental improvements have plateaued and that fundamentally new optimization approaches are needed.

High-performance computing (HPC) facilities intensify this challenge. Exascale supercomputers such as Frontier at Oak Ridge National Laboratory operate at power levels of 8–30 MW, employ 100% direct liquid cooling with variable-speed pumps circulating thousands of liters per minute, and experience rapid thermal transients driven by workload dynamics (Sun et al., 2024; Karimi et al., 2024). These systems differ structurally from enterprise data centers: cooling loops have response times measured in minutes, thermal loads fluctuate on the scale of seconds, and equipment constraints such as pump ramp-rate limits are operationally binding. Despite the scale of energy involved, systematic cooling system optimization for HPC facilities remains largely unexplored. Existing work on Frontier has focused on operational data collection (Sun et al., 2024), power management (Karimi et al., 2024), thermal stability (Grant et al., 2026), and waste heat recovery (Wang et al., 2024). A data-driven machine learning framework for Frontier was developed to quantify cooling inefficiency using gradient-boosting surrogate models, identifying approximately 85 MWh of annual excess cooling energy (Jadhav and Liu, 2026). However, no study has coupled a physics-based digital twin of an exascale cooling system with systematic optimization, nor has any work formally quantified how much of the theoretical energy savings survive when practical operational constraints are imposed.

This paper addresses that question through three co-equal contributions: (i) a validated Modelica-based digital twin of Frontier’s liquid cooling system, (ii) a layered optimization framework using classical gradient-based methods that progressively reveals the sources and magnitudes of energy savings, and (iii) a formally defined implementability gap metric that quantifies the energy savings lost when theoretical optima must accommodate practical operational constraints. The remainder of this section reviews the relevant literature across

four domains and positions the present work within identified research gaps.

## 1.1 *Data center cooling system optimization: approaches and limitations*

Research on data center cooling system optimization has accelerated considerably since a 40% reduction in Google’s cooling energy was reported using neural network recommendations (Evans and Gao, 2016). Although that claim has been critiqued for its lack of peer review and reproducibility (Lazic et al., 2018), it catalyzed substantial academic and industrial interest in intelligent cooling control.

**Reinforcement learning (RL)** approaches treat the cooling system as a Markov decision process and learn control policies from interaction with the environment or a simulator. Deep RL has been demonstrated for data center cooling with promising results on simulated workloads (Li et al., 2020), and a multi-agent RL framework integrated with a digital twin has shown potential for coordinated cooling control (Sarkar et al., 2024). More recently, 14–21% energy savings were reported from offline RL deployed in a production data center, representing one of the few validated real-world implementations (Zhan et al., 2025). RL methods offer the advantage of learning directly from data without requiring an explicit system model, but they introduce challenges around sample efficiency, safety during exploration, and interpretability of the learned policy, all of which are particularly acute in safety-critical HPC environments. More broadly, data-driven surrogates (including gradient boosting models) have been applied to diagnose cooling inefficiency at HPC facilities (Jadhav and Liu, 2026), but these approaches identify waste rather than prescribing constrained optimal control trajectories.

**Model predictive control (MPC)** formulates cooling system optimization as a receding-horizon constrained optimization problem, typically requiring a dynamical model of the thermal system. MPC has been applied to Google’s data centers, achieving a rigorously documented 17.9% cost reduction (Lazic et al., 2018). A foundational framework for stochastic MPC in building climate control was established for commercial buildings (Oldewurtel et al., 2012), and MPC has been demonstrated specifically for chiller plant operation (Ma et al., 2012). MPC naturally handles constraints and can incorporate weather forecasts, but its performance degrades substantially with model uncertainty. Simple rule-based

control has been shown to outperform MPC when model uncertainty exceeds approximately 67% (Maasoumy et al., 2014), highlighting a practical limitation that is often overlooked.

**Classical gradient-based optimization** methods such as Sequential Quadratic Programming (SQP) solve constrained nonlinear programs using gradient information and are the workhorse of engineering design optimization (Kraft, 1988). These methods are deterministic, computationally transparent, and handle equality and inequality constraints through well-understood Lagrangian and active-set strategies. For cooling systems governed by smooth physics (e.g., the cubic affinity law relating pump power to flow rate), the optimization landscape is well suited to gradient methods. Despite these advantages, classical gradient-based optimization is notably absent from the data center and HPC cooling literature. The field has overwhelmingly favored RL and MPC, leaving a significant methodological gap.

Table 1 summarizes the positioning of representative works across these three families, together with the present study. No existing paper simultaneously addresses physics-based digital twin modeling, systematic optimization, HPC liquid cooling, explicit practical constraints, and a formal implementability metric.

Table 1: Comparison of representative cooling system optimization studies. Abbreviations: DT = digital twin; HPC = high-performance computing; DC = data center.

| <b>Study</b>          | <b>Method</b>          | <b>Application</b>    | <b>DT</b>       | <b>Constraints</b> | <b>Gap metric</b> |
|-----------------------|------------------------|-----------------------|-----------------|--------------------|-------------------|
| Evans and Gao (2016)  | Neural net             | Google DC             | No              | No                 | No                |
| Lazic et al. (2018)   | MPC                    | Google DC             | No              | Partial            | No                |
| Li et al. (2020)      | Deep RL                | Enterprise DC         | No              | No                 | No                |
| Sarkar et al. (2024)  | Multi-agent RL         | Enterprise DC         | Yes             | No                 | No                |
| Zhan et al. (2025)    | Offline RL             | Production DC         | No              | Partial            | No                |
| Zhu and Lin (2024)    | Real-time opt.         | Enterprise DC         | Yes             | Partial            | No                |
| Jadhav and Liu (2026) | ML surrogate           | Frontier (HPC)        | No              | No                 | No                |
| Brewer et al. (2024)  | — (V&V only)           | Frontier (HPC)        | Modelica        | —                  | No                |
| Fu et al. (2019)      | — (Sim. only)          | Air-cooled DC         | Modelica        | —                  | No                |
| <b>This study</b>     | <b>SLSQP (layered)</b> | <b>Frontier (HPC)</b> | <b>Modelica</b> | <b>Ramp-rate</b>   | <b>Yes</b>        |

## 1.2 *Digital twins for thermal system modeling and optimization*

The digital twin concept, originally articulated for product lifecycle management (Grieves and Vickers, 2017) and subsequently formalized for industrial applications (Tao et al., 2019), has found growing adoption in building and data center energy systems. The IISE community has recognized digital twins as a transformative methodology for design and manufacturing (Knapp et al., 2020; Tan and Matta, 2024), with active research spanning synchronization, fidelity, and optimization. Digital twins for thermal systems generally follow one of three paradigms: physics-based models that encode conservation laws and constitutive relations, data-driven models that learn input-output mappings from operational data, and hybrid approaches that combine both (Afram and Janabi-Sharifi, 2014). For optimization applications where control strategies must be explored beyond the range of historical operating data, physics-based models offer superior generalization and physical interpretability.

The Modelica language and its associated Buildings Library (Wetter et al., 2014) have emerged as the dominant open-source platform for equation-based modeling of HVAC and cooling systems. This library provides validated component models for heat exchangers, pumps, valves, pipes, and control systems that can be composed into arbitrarily complex system topologies. The first comprehensive Modelica-based data center cooling models were developed for a conventional air-cooled facility with computer room air handlers (Fu et al., 2019,?). Modelica modeling has been extended to district cooling systems (Hinkelman et al., 2022), and open-source Modelica models for chiller plants with water-side economizers have reported energy savings of 8.6–36.8% across operating scenarios (Fan et al., 2021). More recently, Modelica has been used for comparative co-design of data center cooling controls (Grahovac et al., 2023), and the Buildings Library has been coupled with EnergyPlus through the Spawn framework (Wetter et al., 2024).

For HPC cooling specifically, the Exascale Digital Twin (ExaDigiT) project at Oak Ridge National Laboratory developed a digital twin framework for liquid-cooled supercomputers using the TRANSFORM library within the Modelica environment (Brewer et al., 2024; Kumar et al., 2024; Greenwood et al., 2024). ExaDigiT models the thermo-fluid dynamics of Frontier’s cooling loops and has been validated against operational sensor data. However, the ExaDigiT effort focused on verification and validation of the digital twin itself;

it did not proceed to use the twin for systematic cooling optimization. This pattern recurs across the literature: several groups have built physics-based cooling models (Fu et al., 2019; Hinkelman et al., 2022) or digital twin frameworks (Athavale et al., 2024; Sarkar et al., 2024), but the step from validated model to actionable optimization is frequently omitted or treated superficially.

The present work constructs an independent Modelica-based digital twin of Frontier’s cooling system, distinct from ExaDigiT in both modeling approach and purpose. ExaDigiT employs the TRANSFORM library and targets broad digital twin capabilities including real-time monitoring and what-if analysis; the model developed here uses the Modelica Buildings Library (Wetter et al., 2014) and is purpose-built for steady-state optimization. The model is calibrated against 47,186 validated operational records from a published operational dataset (Sun et al., 2024) and validated to ASHRAE Guideline 14 (ASHRAE, 2014) criteria, achieving coefficient of variation of the root mean square error (CV-RMSE) values of 1.96–2.67% and normalized mean bias error (NMBE) within  $\pm 10\%$  across all monitored variables (Section 2.3). This level of validation provides the confidence necessary to trust optimization results derived from the model.

### ***1.3 The implementability gap: from theoretical optima to practical control***

A persistent challenge in cooling system optimization is the gap between what is theoretically optimal and what can be practically implemented. This gap arises from multiple sources: actuator limitations (pumps and valves cannot change state instantaneously), thermal inertia (large fluid volumes resist rapid temperature changes), safety margins (component temperatures must remain within rated bounds during transients), and operational protocols (facility operators require gradual, predictable system behavior). Despite the practical importance of these constraints, the literature lacks a formal framework for quantifying their effect on achievable energy savings.

The closest conceptual precedents come from three distinct and largely disconnected research areas. In building energy research, the performance gap between predicted and measured energy consumption has been extensively documented, with discrepancies of 20–550% reported across building types (de Wilde, 2014; Van Dronkelaar et al., 2016). How-

ever, this performance gap refers to the mismatch between design-stage predictions and as-built operation, not between optimal and implementable control strategies. In robotics and reinforcement learning, the simulation-to-real gap (also called the reality gap) describes the degradation in controller performance when policies trained in simulation are transferred to physical systems (Salvato et al., 2021; Zhao et al., 2020). This has been addressed specifically for building HVAC RL, but without defining a quantitative metric (Chen et al., 2020). In energy storage optimization, imposing ramp-rate constraints of 10% of maximum capacity has been shown to reduce arbitrage profit by 10–35% (Hashmi et al., 2024), with constrained solutions retaining 65–90% of unconstrained profit. This represents the closest quantitative analog to our work, but it addresses battery storage rather than cooling systems.

None of these research areas formally defines a metric for the gap between unconstrained optimal control and practically implementable control in cooling systems. We address this by introducing the implementability gap, defined as the fraction of theoretical optimal energy savings that cannot be captured due to practical operational constraints, and its complement, the recovery ratio, which quantifies the fraction of theoretical savings that remain achievable (Section 2.4.4). This framework is operationalized through a layered optimization approach: Strategy A (flow-only optimization) establishes a conservative baseline by optimizing only pump speeds; Strategy B (unconstrained co-optimization) simultaneously optimizes pump speeds and cooling tower fan operation without operational constraints, revealing the theoretical maximum savings; and Strategy C (ramp-constrained co-optimization) re-introduces ramp-rate limits on all actuators, yielding the practically implementable savings. The difference between Strategies B and C directly measures the implementability gap, while the ratio of Strategy C savings to Strategy B savings gives the recovery ratio.

This layered design serves a dual purpose. Methodologically, it isolates the contribution of each optimization degree of freedom and each constraint, providing insight that a single monolithic optimization would obscure. Practically, it gives facility operators a transparent menu of strategies with clearly quantified trade-offs between theoretical savings and implementation complexity.

## 1.4 Contributions and paper organization

The contributions of this paper are as follows:

1. A validated Modelica-based digital twin of the Frontier supercomputer’s three-loop liquid cooling system, independently developed using the Modelica Buildings Library, calibrated against one year of operational data (47,186 records), and validated to ASHRAE Guideline 14 criteria with CV-RMSE of 1.96–2.67%.
2. A layered optimization framework comprising three strategies of increasing complexity (flow-only, unconstrained co-optimization, and ramp-constrained co-optimization) implemented using SLSQP, representing the first application of classical gradient-based optimization to HPC cooling systems.
3. The implementability gap metric and recovery ratio, formal measures of the energy savings lost (and retained) when practical ramp-rate constraints are imposed on theoretically optimal control strategies. To the authors’ knowledge, this is the first such metric defined for cooling system optimization.
4. Operational insights for exascale cooling, including the finding that flow-only optimization achieves 20.4% pumping energy savings, unconstrained co-optimization reaches 30.1%, and ramp-constrained co-optimization retains 27.8% (corresponding to a recovery ratio of 92.4%), demonstrating that the majority of theoretical savings are practically recoverable.

The remainder of this paper is organized as follows. Section 2 presents the digital twin model, including the system architecture, governing equations, calibration procedure, and validation protocol. Section 3 presents the validation results, optimization findings, and energy savings across strategies. Section 4 discusses system-level insights, practical implementability, robustness, limitations, and directions for future work. Section 5 concludes with principal findings.

## 2 Methodology

This section presents the digital twin modeling framework and optimization formulation developed for the Frontier supercomputer cooling system. Section 2.1 describes the physical

cooling architecture and the digital twin concept. Section 2.2 formulates the physics-based sub-models. Section 2.3 defines the calibration procedure and validation criteria. Section 2.4 presents the three optimization strategies in a layered formulation.

## 2.1 System description and digital twin architecture

### 2.1.1 Frontier cooling system

The Frontier supercomputer at Oak Ridge National Laboratory (ORNL) is an exascale high-performance computing (HPC) system, achieving 1.102 exaFLOPS on the HPL benchmark (Sun et al., 2024). Frontier employs a warm-water liquid cooling architecture comprising three thermally coupled fluid loops arranged in a cascaded heat rejection path, with operational waste heat ranging from 8 to 28 MW depending on computational workload, as illustrated in Figure 1.

The *tertiary loop* (also called the coolant distribution unit, or CDU, loop) circulates a 50/50 ethylene glycol-water mixture (reported as a 50% solution with the basis unspecified (Sun et al., 2024); see Section 2.3.2 for calibration details) directly through the compute cabinets. Twenty-five CDUs serve 74 compute cabinets, rejecting waste heat from the processors and accelerators into the glycol coolant. The heated glycol is then passed through plate heat exchangers that transfer the thermal energy to the *secondary loop* (the hot-temperature water (HTW) loop), which circulates pure water at flow rates between 113 and 412 kg/s depending on operating conditions. The HTW loop in turn rejects heat to the *primary loop* (the cooling tower water (CTW) loop) through a second set of heat exchangers, and the CTW loop dissipates the heat to the atmosphere via mechanical-draft cooling towers.

A defining feature of the Frontier cooling architecture is that the HTW system is organized into four parallel subloops, of which three are active and one is held in reserve (Sun et al., 2024). Each active subloop contains its own CDU cluster, HTW pump, and heat exchanger. The nominal flow distribution across the three active subloops is approximately 24.6%, 26.0%, and 49.5% of the total HTW flow, as derived from the operational dataset and verified by the Modelica simulation (Section 3). This parallel topology is critical to the optimization formulation because the thermal constraint must be satisfied independently

in each branch: the return temperature in every subloop must remain below the equipment limit regardless of conditions in the other two branches.

The operational dataset provides records at 10-minute intervals (Sun et al., 2024) spanning the full calendar year 2023. The dataset includes supply and return temperatures, per-subloop flow rates and heat loads, and aggregate power consumption. After removing sensor anomalies, maintenance shutdowns, and physically inconsistent records (return temperature below supply temperature, heat load exceeding 15 MW, supply temperature below 5°C, or total flow below 30 kg/s), 47,186 validated operating points remain for model development and optimization.

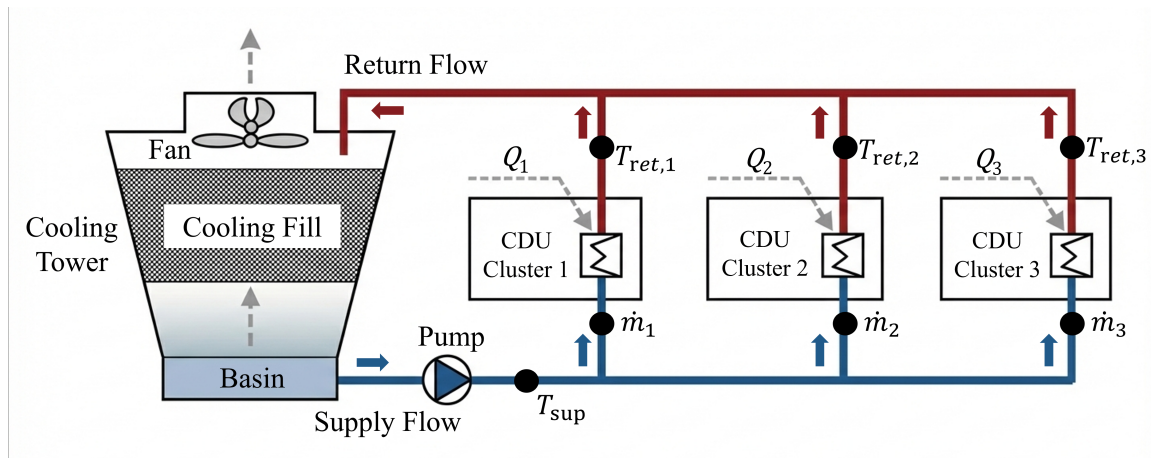


Figure 1: Schematic of the Frontier supercomputer cooling architecture. The HTW system comprises three parallel subloops, each serving dedicated CDU clusters through plate heat exchangers. A variable-speed pump drives the supply flow from the cooling tower basin through the subloops, and warm return flow is rejected to the atmosphere via a mechanical-draft cooling tower. State variables used in the digital twin model are annotated at measurement points.

### 2.1.2 Digital twin framework

The digital twin developed in this work serves as a simulation-based optimization testbed: a calibrated physics model that can evaluate candidate control strategies offline, using historical operating data as boundary conditions, before any physical implementation. Figure 2 illustrates the overall framework, which consists of three layers.

The *physical layer* comprises the Frontier cooling plant and its supervisory control system, which currently operates the HTW pumps at fixed-speed setpoints. The *digital twin layer* is a physics-based Modelica model implemented in OpenModelica using components from the Buildings Library (Wetter et al., 2014). The model ingests measured boundary conditions (heat loads, supply temperature, and flow rates) and predicts system-level thermal and energy performance. The *optimization layer* formulates and solves energy minimization problems using the digital twin’s analytical prediction equations as the plant model, subject to thermal safety constraints derived from equipment specifications.

The key advantage of this architecture is that the optimization operates on the same physics equations used in the validated digital twin, ensuring consistency between the model used for control design and the model used for performance prediction. This avoids the simulation-to-real gap that arises when surrogate models (e.g., neural networks) are used for optimization but validated against a different simulator.

## 2.2 *Physics-based model formulation*

The digital twin represents the Frontier HTW cooling system using three coupled sub-models: heat exchangers connecting the CDU, HTW, and CTW loops; variable-speed pumps driving the HTW flow; and mechanical-draft cooling towers rejecting heat to the atmosphere. Each sub-model is formulated below, with notation defined at first use.

### 2.2.1 *Heat exchanger model*

Each subloop’s CDU-to-HTW heat exchanger is modeled using the effectiveness-NTU ( $\varepsilon$ -NTU) method (Incropera et al., 2007). For a counterflow plate heat exchanger with known effectiveness  $\varepsilon_i$ , the return temperature in subloop  $i$  at timestep  $t$  is determined by the energy balance:

$$T_{\text{ret},i}(t) = T_{\text{sup}}(t) + \frac{Q_i(t)}{f_i \cdot \dot{m}(t) \cdot c_p} \quad (1)$$

where  $f_i$  is the fraction of total flow through subloop  $i$ . This expression follows directly from the first law of thermodynamics applied to the coolant stream passing through the CDU cluster, under the assumption that all waste heat  $Q_i$  is absorbed by the HTW fluid. The flow fractions are determined by the parallel hydraulic network topology and remain

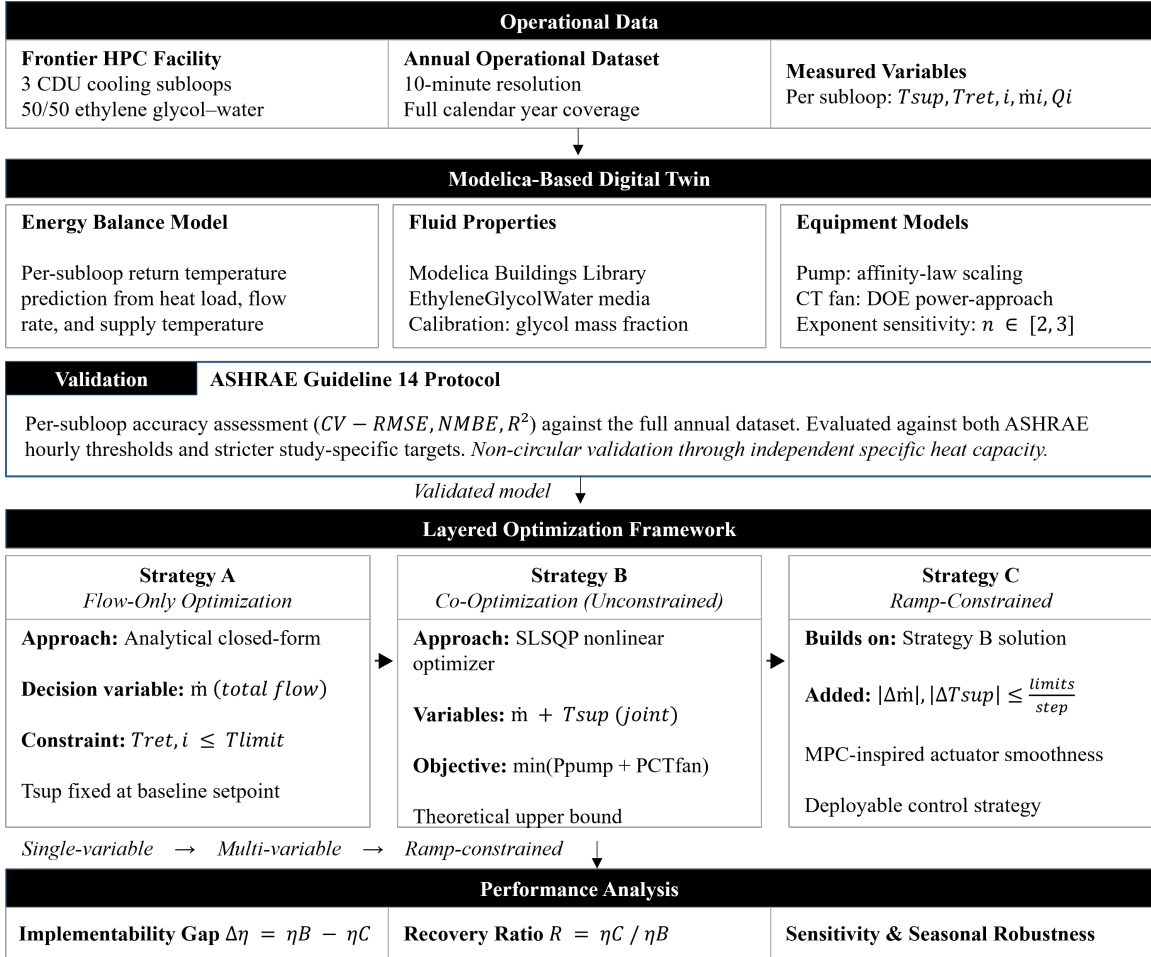


Figure 2: Digital twin framework for cooling system optimization. The physical layer provides operational data, the Modelica-based digital twin predicts thermal and energy performance, and the optimization layer determines energy-minimal control setpoints subject to thermal safety constraints.

approximately constant at  $f_1 = 0.244$ ,  $f_2 = 0.258$ , and  $f_3 = 0.498$  across the full operating range, as derived from the operational dataset and confirmed by the Modelica hydraulic model (Section 3).

The HTW-to-CTW heat exchangers connecting the secondary and primary loops are modeled using a constant-effectiveness formulation (`ConstantEffectiveness` component in the Modelica Buildings Library; Wetter et al., 2014), which represents the plate heat exchangers as idealized devices with prescribed thermal effectiveness:

$$Q_{\text{HX}} = \varepsilon \cdot C_{\min} \cdot (T_{\text{hot,in}} - T_{\text{cold,in}}) \quad (2)$$

where  $C_{\min} = \min(\dot{m}_{\text{hot}}c_{p,\text{hot}}, \dot{m}_{\text{cold}}c_{p,\text{cold}})$  is the minimum heat capacity rate and  $\varepsilon$  is the heat exchanger effectiveness. The nominal effectiveness values used in the model are  $\varepsilon_{\text{CDU-HTW}} = 0.65$  and  $\varepsilon_{\text{HTW-CTW}} = 0.75$ , consistent with the temperature profiles observed in the Frontier dataset.

To enable closed-form optimization (Section 2.4), the heat exchanger thermal resistance is characterized by an aggregate overall heat transfer coefficient-area product  $UA$ . Under the assumption that the HTW-side convective resistance dominates the overall thermal resistance (i.e., wall conduction and CTW-side resistance are comparatively small), the Dittus-Boelter correlation for turbulent internal flow yields  $h \propto \dot{m}^{0.8}$  (Incropera et al., 2007), and consequently:

$$UA(\dot{m}) = UA_{\text{nom}} \left( \frac{\dot{m}}{\dot{m}_{\text{nom}}} \right)^{0.8} \quad (3)$$

where  $UA_{\text{nom}} = 2,252 \text{ kW/K}$  is the nominal value at the reference flow rate  $\dot{m}_{\text{nom}} = 190 \text{ kg/s}$ . This scaling relationship is used in the back-calculation of cooling tower water supply temperature from measured HTW conditions (Section 2.3).

### 2.2.2 Pump power model

The HTW pumps are modeled using the affinity laws for variable-speed centrifugal pumps. For a closed-loop system with negligible static head (as in the Frontier HTW loop, where the pressure drop is dominated by pipe friction and component losses), the system curve is purely quadratic and the pump power relates to flow rate as:

$$P_{\text{pump}}(\dot{m}) = P_{\text{pump,nom}} \left( \frac{\dot{m}}{\dot{m}_{\text{nom}}} \right)^n \quad (4)$$

The baseline pump power exponent is  $n = 3$ , corresponding to the theoretical cubic law ( $P \propto N^3$ ,  $Q \propto N$ , hence  $P \propto Q^3$ ) for variable-speed operation against a purely quadratic system curve (ASHRAE, 2020). In practice, the exponent may deviate from 3 due to residual static head, valve characteristics, and motor efficiency variations. The sensitivity of the optimization results to the pump exponent is examined in Section 3 for  $n \in \{2.0, 2.5, 3.0\}$ .

The nominal pump power  $P_{\text{pump,nom}}$  is calibrated from the Frontier dataset by matching the measured total accessory power at the reference operating point. At the Frontier facility, the HTW pumps currently operate at fixed-speed setpoints: approximately 200 kg/s during the winter months (November through April) and 350–400 kg/s during the summer months (May through October). This step-like operating pattern, rather than a continuous modulation proportional to thermal demand, represents the primary source of energy waste that the proposed optimization addresses.

### 2.2.3 Cooling tower model

The mechanical-draft cooling towers reject heat from the CTW loop to the atmosphere. The cooling tower outlet temperature is modeled using a fixed-approach formulation:

$$T_{\text{CT,out}} = T_{\text{wb}} + \Delta T_{\text{app}} \quad (5)$$

where  $T_{\text{wb}}$  is the ambient wet-bulb temperature and  $\Delta T_{\text{app}}$  is the approach temperature, which is the minimum temperature difference between the cooled water leaving the tower and the ambient wet-bulb. A nominal approach of 4°C is used, consistent with values reported for large-scale data center cooling installations (ASHRAE, 2020).

The cooling tower fan power is modeled as a function of the heat rejection rate and the temperature driving potential:

$$P_{\text{CT}} = P_{\text{CT,nom}} \left( \frac{Q_{\text{rej}}}{Q_{\text{rej,nom}}} \right) \left( \frac{\Delta T_{\text{app,nom}}}{\Delta T_{\text{app}}} \right)^\gamma \quad (6)$$

where  $Q_{\text{rej}}$  is the actual heat rejection rate,  $Q_{\text{rej,nom}}$  is the design heat rejection rate, and  $\gamma = 1.0$  is the fan power scaling exponent. The heat rejected by the cooling tower equals the total IT heat load plus the pump work added to the fluid:

$$Q_{\text{rej}} = \sum_{i=1}^3 Q_i + P_{\text{pump}} \quad (7)$$

The total cooling system power consumption is the sum of pump and cooling tower fan power:

$$P_{\text{total}} = P_{\text{pump}} + P_{\text{CT}} \quad (8)$$

This formulation captures a fundamental trade-off: reducing pump flow lowers  $P_{\text{pump}}$  (cubic relationship) but raises the return temperature, which narrows the approach temperature and increases  $P_{\text{CT}}$ . The optimization must navigate this coupling to minimize total system energy.

## 2.3 Model calibration and validation approach

### 2.3.1 Modelica implementation

The physics-based model is implemented in OpenModelica 1.23 using the Modelica Buildings Library v11 (Wetter et al., 2014). The implementation uses the following key components: `Buildings.Fluid.HeatExchangers.ConstantEffectiveness` for modeling the plate heat exchangers as constant-effectiveness devices; as for the variable-speed pumps, use `Buildings.Fluid.Movers.FlowControlled_m_flow`; for the hydraulic resistance elements that produce the target flow distribution across the three parallel branches, use `Buildings.Fluid.FixedResistances.PressureDrop`; and for the glycol-water fluid properties based on polynomial correlations for secondary working fluids (Melinder, 2010), use `Buildings.Media.Antifreeze.EthyleneGlycolWater`.

### 2.3.2 Fluid property calibration

A single calibration parameter governs the model’s accuracy: the effective glycol mass fraction  $X_a$  in the ethylene glycol-water mixture. The original dataset reports a 50/50 ethylene glycol-water coolant without specifying whether this refers to a mass or volumetric ratio (Sun et al., 2024). coolant without specifying whether this refers to a mass or volumetric ratio. Analysis of the dataset reveals that the waste-heat columns are derived quantities, computed internally as  $Q_i = \dot{m}_i c_p (T_{\text{ret},i} - T_{\text{sup}})$  with a fixed conversion constant of  $c_p = 3,709 \text{ J}/(\text{kg}\cdot\text{K})$  and a flow conversion factor of  $0.0631 \text{ kg}/(\text{s}\cdot\text{gpm})$ . This constant is applied uniformly across all 49,869 records with zero variance, confirming that  $Q$  is not

an independent measurement. Consequently, using  $c_p = 3,709 \text{ J}/(\text{kg}\cdot\text{K})$  to predict return temperatures from  $Q$  would recover the dataset’s own formula, a circular validation.

To avoid this circularity, the digital twin adopts  $c_p = 3,500 \text{ J}/(\text{kg}\cdot\text{K})$ , the standard engineering value for 50/50 ethylene glycol-water at operating temperatures (25–35 °C). In the Modelica model, the Buildings Library’s `EthyleneGlycolWater` media package takes  $X_a$  as a mass fraction and yields  $c_p \approx 3,190 \text{ J}/(\text{kg}\cdot\text{K})$  at  $X_a = 0.50$  (reference temperature 30 °C). Setting  $X_a = 0.40$  yields  $c_p \approx 3,500 \text{ J}/(\text{kg}\cdot\text{K})$ , aligning the Modelica fluid properties with the adopted validation constant. This adjustment is physically consistent with an effective volumetric fraction of approximately 50% when accounting for the density difference between ethylene glycol (1,113 kg/m<sup>3</sup>) and water (998 kg/m<sup>3</sup>) at 30 °C. The 6% gap between the adopted  $c_p$  and the dataset’s internal constant (3,500 vs. 3,709) produces the validation errors reported in Section 3.1; this gap represents a genuine test of the model’s predictive capability rather than a numerical artefact. The sensitivity of the optimization results to  $c_p$  uncertainty is minimal because the optimizer uses the same property correlations as the digital twin, so any systematic offset cancels in the relative comparison between baseline and optimized performance.

### 2.3.3 Validation protocol

The model is validated against measured data following ASHRAE Guideline 14-2014 (ASHRAE, 2014), which defines acceptance criteria for calibrated simulation models (note: superseded by Guideline 14-2023; the 2014 edition is used here for consistency with the majority of published digital twin validation studies). Two primary metrics are used:

The CV-RMSE quantifies the overall prediction scatter:

$$\text{CV-RMSE} = \frac{1}{\bar{y}} \sqrt{\frac{\sum_{t=1}^n (y_t - \hat{y}_t)^2}{n - p}} \times 100\% \quad (9)$$

The Normalized Mean Bias Error (NMBE) quantifies systematic over- or under-prediction:

$$\text{NMBE} = \frac{\sum_{t=1}^n (y_t - \hat{y}_t)}{(n - p) \cdot \bar{y}} \times 100\% \quad (10)$$

where  $y_t$  and  $\hat{y}_t$  are the measured and predicted values at timestep  $t$ ,  $\bar{y}$  is the mean of the measured values,  $n$  is the number of observations, and  $p$  is the number of adjustable model parameters ( $p = 1$  for calibrated simulation per ASHRAE Guideline 14 (ASHRAE, 2014)).

ASHRAE Guideline 14 specifies acceptance thresholds of  $\text{CV-RMSE} \leq 30\%$  and  $|\text{NMBE}| \leq 10\%$  for hourly data. To ensure a stringent test of model fidelity, we adopt stricter targets of  $\text{CV-RMSE} \leq 5\%$  and  $|\text{NMBE}| \leq 5\%$  for the per-subloop return temperature predictions.

The validation is conducted using a system identification approach: measured supply temperature  $T_{\text{sup}}(t)$ , per-subloop flow rates  $f_i \cdot \dot{m}(t)$ , and per-subloop heat loads  $Q_i(t)$  are prescribed as boundary conditions, and the model predicts the per-subloop return temperatures  $T_{\text{ret},i}(t)$ . This isolates the heat transfer physics as the quantity being validated, removing uncertainty in pump performance and cooling tower behavior from the validation assessment. Two representative one-week periods are selected for detailed analysis: a summer week (July 1–7) representing peak thermal stress with supply temperatures reaching  $33.6^\circ\text{C}$  and flows up to  $412 \text{ kg/s}$ , and a winter week (January 7th–14th) representing part-load conditions with supply temperatures as low as  $10.6^\circ\text{C}$  and flows down to  $113 \text{ kg/s}$ . Validation results are presented in Section 3.1.

## 2.4 Optimization formulation

The objective of the cooling system optimization is to minimize the total annual energy consumption of the HTW cooling infrastructure while maintaining thermal safety for the compute equipment. The equipment manufacturer specifies a maximum coolant return temperature of  $45^\circ\text{C}$ . To provide an operational safety margin, the optimization enforces a constraint of  $T_{\text{ret},i} \leq 42^\circ\text{C}$  in each subloop, corresponding to a  $3^\circ\text{C}$  buffer below the equipment limit.

Three optimization strategies are formulated in a layered progression, where each subsequent strategy extends the preceding one by adding decision variables or constraints. This structure enables a systematic evaluation of the trade-offs between theoretical optimality, operational complexity, and implementability.

### 2.4.1 Strategy A: Flow-only optimization

Strategy A optimizes only the HTW pump flow rate while keeping the supply temperature at its measured baseline value. The formulation is:

$$\min_{m(t)} P_{\text{total}}(m(t), T_{\text{sup}}^{\text{base}}(t)) \quad (11a)$$

$$\text{s.t. } T_{\text{ret},i}(m(t), T_{\text{sup}}^{\text{base}}(t)) \leq T_{\text{limit}}, \quad i = 1, 2, 3 \quad (11b)$$

$$m_{\text{min}} \leq m(t) \leq m_{\text{max}} \quad (11c)$$

where  $T_{\text{limit}} = 42^\circ\text{C}$ ,  $m_{\text{min}} = 30$  kg/s (minimum stable pump operation), and  $m_{\text{max}} = 420$  kg/s (maximum pump capacity). The supply temperature  $T_{\text{sup}}^{\text{base}}(t)$  is the measured value at each timestep and is not a decision variable in this formulation.

For Strategy A, the thermal constraint (11b) admits an analytical solution. Substituting the energy balance (1) into the constraint and solving for the minimum feasible flow yields:

$$m_{\text{min}}^{\text{thermal}}(t) = \max_{i \in \{1,2,3\}} \frac{Q_i(t)}{f_i \cdot c_p \cdot (T_{\text{limit}} - T_{\text{sup}}^{\text{base}}(t))} \quad (12)$$

The binding constraint is determined by the subloop with the highest heat load relative to its flow fraction. In the Frontier system, the mean heat load fractions are  $Q_1/Q_{\text{total}} \approx 0.181$ ,  $Q_2/Q_{\text{total}} \approx 0.194$ , and  $Q_3/Q_{\text{total}} \approx 0.625$ , while the corresponding flow fractions are  $f_1 = 0.246$ ,  $f_2 = 0.260$ , and  $f_3 = 0.495$ . Subloop 3 carries approximately 63% of the total heat load through 49.5% of the total flow, reflecting its higher mean temperature differential ( $\overline{\Delta T}_3 = 13.8^\circ\text{C}$  vs.  $\overline{\Delta T}_{1,2} \approx 8^\circ\text{C}$ ). This makes it the binding branch at virtually every operating point. The optimal flow is then:

$$m^*(t) = \max\{m_{\text{min}}, m_{\text{min}}^{\text{thermal}}(t)\} \quad (13)$$

This closed-form solution eliminates the need for iterative numerical optimization and guarantees zero constraint violations by construction.

### 2.4.2 Strategy B: Unconstrained co-optimization

Strategy B extends Strategy A by introducing the supply temperature setpoint  $T_{\text{sp}}$  as a second decision variable. The physical mechanism is that raising the supply temperature reduces the heat rejection burden on the cooling towers (by narrowing the temperature

difference that drives tower heat transfer), at the cost of reducing the thermal headroom available for pump flow reduction. The formulation is:

$$\min_{m(t), T_{\text{sp}}(t)} P_{\text{total}}(m(t), T_{\text{sp}}(t)) \quad (14\text{a})$$

$$\text{s.t. } T_{\text{ret},i}(m(t), T_{\text{sp}}(t)) \leq T_{\text{limit}}, \quad i = 1, 2, 3 \quad (14\text{b})$$

$$m_{\text{min}} \leq m(t) \leq m_{\text{max}} \quad (14\text{c})$$

$$T_{\text{sp},\text{min}} \leq T_{\text{sp}}(t) \leq T_{\text{sp},\text{max}} \quad (14\text{d})$$

where  $T_{\text{sp},\text{min}} = 10^\circ\text{C}$  and  $T_{\text{sp},\text{max}} = 35^\circ\text{C}$  bound the feasible supply temperature range. Unlike Strategy A, the two-variable problem does not admit a simple closed-form solution because of the nonlinear coupling between  $m$  and  $T_{\text{sp}}$  in both the pump power Equation (4) and the cooling tower power Equations (6–7). Strategy B is solved using Sequential Least-Squares Programming (SLSQP) (Kraft, 1988) at each timestep independently, treating each 10-minute interval as a quasi-steady-state optimization.

Strategy B represents the theoretical upper bound on achievable savings because it optimizes both available control degrees of freedom without imposing actuator constraints. However, the resulting control trajectories may exhibit large step-to-step changes in both flow rate and supply temperature, which are impractical for real-time implementation due to water hammer risk, thermal shock to equipment, and variable-frequency drive slew rate limitations.

### 2.4.3 Strategy C: Ramp-constrained co-optimization

Strategy C addresses the implementability gap by augmenting the Strategy B formulation with ramp-rate constraints that limit the step-to-step change in both decision variables.

The formulation is:

$$\min_{m(t), T_{\text{sp}}(t)} P_{\text{total}}(m(t), T_{\text{sp}}(t)) \quad (15\text{a})$$

$$\text{s.t. } T_{\text{ret},i}(m(t), T_{\text{sp}}(t)) \leq T_{\text{limit}}, \quad i = 1, 2, 3 \quad (15\text{b})$$

$$m_{\text{min}} \leq m(t) \leq m_{\text{max}} \quad (15\text{c})$$

$$T_{\text{sp},\text{min}} \leq T_{\text{sp}}(t) \leq T_{\text{sp},\text{max}} \quad (15\text{d})$$

$$|m(t) - m(t-1)| \leq \Delta m_{\text{max}} \quad (15\text{e})$$

$$|T_{\text{sp}}(t) - T_{\text{sp}}(t-1)| \leq \Delta T_{\text{max}} \quad (15\text{f})$$

The ramp-rate limits are set to  $\Delta m_{\text{max}} = 50$  kg/s per 10-minute step and  $\Delta T_{\text{max}} = 1^\circ\text{C}$  per 10-minute step. These values are operational constraints reflecting thermal management requirements for large-scale hot-water distribution systems: the flow ramp limit of 50 kg/s per step corresponds to a maximum rate of change of 5 kg/s per minute, which provides adequate margin against water hammer and pressure transients in the piping network while remaining well within the response capability of modern variable-frequency drives (ASHRAE, 2020). The temperature ramp limit of  $1^\circ\text{C}$  per step prevents thermal shock to the heat exchangers and ensures that downstream CDU control loops can track the setpoint change without oscillation.

The ramp constraints (15e)–(15f) introduce temporal coupling between successive timesteps: the feasible region at timestep  $t$  depends on the solution at timestep  $t-1$ . This transforms the problem from a collection of independent per-timestep optimizations (as in Strategies A and B) into a sequential decision process. The formulation follows the principles of model predictive control (MPC), where the optimizer at each step accounts for the current state (including the previous setpoints) when computing the next control action. Strategy C is solved sequentially using SLSQP with the ramp constraints reformulated as bound tightening: at each timestep, the feasible bounds on  $m$  and  $T_{\text{sp}}$  are narrowed to  $[m(t-1) - \Delta m_{\text{max}}, m(t-1) + \Delta m_{\text{max}}]$  and  $[T_{\text{sp}}(t-1) - \Delta T_{\text{max}}, T_{\text{sp}}(t-1) + \Delta T_{\text{max}}]$ , respectively, intersected with the global bounds.

A safety override is incorporated: if the thermal constraint is violated at the optimal solution (which can occur when the ramp limit prevents the flow from increasing fast enough after a sudden load spike), the flow rate is immediately increased to the minimum thermally

safe value computed by Equation (12), overriding the ramp constraint. This ensures that thermal safety always takes priority over actuator smoothness.

#### 2.4.4 Quantifying the implementability gap

A key metric introduced in this work is the *implementability gap*, defined as the difference in total energy savings between Strategy B (theoretical optimum) and Strategy C (implementable solution):

$$\Delta_{\text{gap}} = \frac{E_{\text{total}}^C - E_{\text{total}}^B}{E_{\text{total}}^{\text{base}}} \times 100\% \quad (16)$$

The corresponding recovery ratio can be calculated as:

$$\eta_{\text{recovery}} = \frac{E_{\text{total}}^{\text{base}} - E_{\text{total}}^C}{E_{\text{total}}^{\text{base}} - E_{\text{total}}^B} \times 100\% \quad (17)$$

where  $E_{\text{total}}^{\text{base}}$ ,  $E_{\text{total}}^B$ , and  $E_{\text{total}}^C$  are the annual total energy consumption under the baseline, Strategy B, and Strategy C, respectively. A high recovery ratio ( $\eta_{\text{recovery}} \rightarrow 100\%$ ) indicates that the ramp constraints impose minimal energy penalty relative to the unconstrained optimum, suggesting that the theoretical savings are largely realizable in practice.

## 3 Results

This section presents the optimization results using a full calendar year (2023) of operational data from the Frontier supercomputer facility at Oak Ridge National Laboratory. The dataset comprises 47,186 validated operating points recorded at 10-minute intervals, after filtering for sensor anomalies and maintenance shutdowns.

### 3.1 Digital twin validation

The digital twin is validated against the full annual dataset ( $n = 47,186$  records after filtering) using the ASHRAE Guideline 14 protocol described in Section 2.3.3. For each subloop  $i$ , the predicted return temperature follows the energy balance Equation (1) with  $c_p = 3,500 \text{ J}/(\text{kg}\cdot\text{K})$ , the standard engineering value for 50/50 ethylene glycol-water at operating temperatures. This value is intentionally distinct from the conversion constant

embedded in the dataset’s waste-heat column ( $c_p = 3,709 \text{ J}/(\text{kg}\cdot\text{K})$ ), ensuring a non-circular validation.

Table 2 reports the per-subloop prediction errors. All three subloops satisfy both the ASHRAE Guideline 14 hourly thresholds ( $\text{CV-RMSE} \leq 30\%$ ,  $|\text{NMBE}| \leq 10\%$ ) and the stricter targets adopted in this study ( $\text{CV-RMSE} \leq 5\%$ ,  $|\text{NMBE}| \leq 5\%$ ). Subloop 3 exhibits the largest CV-RMSE (2.67%) due to its higher mean temperature differential ( $\overline{\Delta T}_3 = 13.8^\circ\text{C}$  vs.  $\overline{\Delta T}_{1,2} \approx 8^\circ\text{C}$ ), which amplifies sensitivity to the assumed  $c_p$ . The positive NMBE across all subloops indicates a consistent over-prediction bias of 0.5–0.9°C, attributable to the 6% difference between the adopted  $c_p$  and the dataset’s internal conversion constant.

Table 2: Digital twin validation: per-subloop return temperature prediction errors evaluated over the full annual dataset ( $n = 47,186$ ;  $p = 1$  calibration parameter).

| Metric                    | Subloop 1 | Subloop 2 | Subloop 3 |
|---------------------------|-----------|-----------|-----------|
| CV-RMSE (%)               | 1.96      | 1.97      | 2.67      |
| NMBE (%)                  | +1.69     | +1.72     | +2.43     |
| RMSE ( $^\circ\text{C}$ ) | 0.551     | 0.558     | 0.907     |
| $R^2$                     | 0.9933    | 0.9927    | 0.9088    |

ASHRAE Guideline 14 thresholds:  $\text{CV-RMSE} \leq 30\%$ ,  $|\text{NMBE}| \leq 10\%$ .  
Stricter targets adopted here:  $\text{CV-RMSE} \leq 5\%$ ,  $|\text{NMBE}| \leq 5\%$ .

### 3.2 Baseline operating conditions

Figure 3 presents the annual operating profile of the Frontier hot-temperature water (HTW) cooling loop across 2023. Three key observations emerge from the data. First, the computational heat load remains relatively stable between 7 and 12 MW throughout the year (Figure 3(a)), reflecting the sustained utilization typical of leadership-class supercomputers. Second, the supply temperature  $T_{\text{supply}}$  varies from approximately  $12^\circ\text{C}$  in winter to  $29^\circ\text{C}$  in summer, tracking the ambient wet-bulb temperature with a roughly constant heat exchanger approach (Figure 3(b)). The return temperature  $T_{\text{return}}$  follows a similar seasonal pattern, with 7-day averages ranging from  $27^\circ\text{C}$  to  $35^\circ\text{C}$ . The dashed horizontal line at  $42^\circ\text{C}$

indicates the optimization constraint threshold, set 3°C below the 45°C equipment limit. Third, and most notably, the pump flow rate exhibits a pronounced step change around May (Figure 3(c)), jumping from approximately 200 kg/s to 350–400 kg/s and remaining elevated through October. This step-like behavior, rather than a smooth modulation proportional to cooling demand, suggests the pumps are operated at fixed-speed setpoints without continuous optimization.

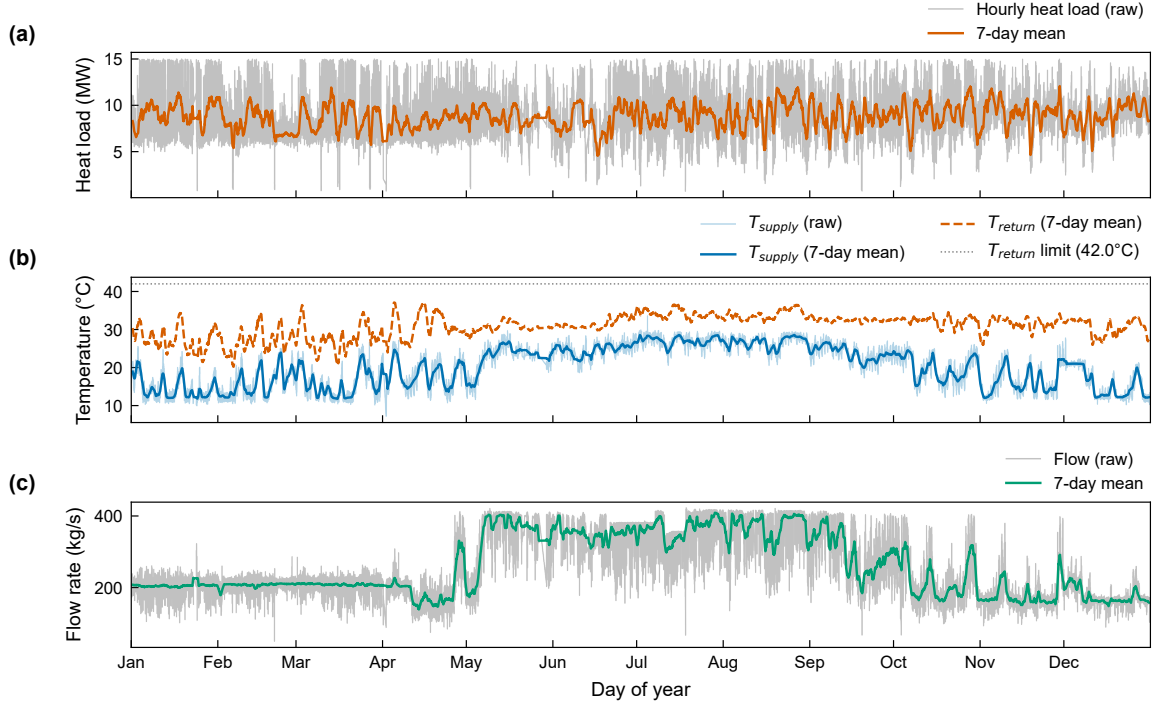


Figure 3: Annual operating conditions for the Frontier HTW cooling loop in 2023: (a) total computational heat load, (b) supply and return temperatures with 42°C constraint threshold, and (c) total pump flow rate. Gray traces show 10-minute data; colored lines show 7-day rolling means.

### 3.3 Over-pumping diagnosis

To quantify the extent of excess pumping, we compare the measured baseline flow rate against the analytical minimum flow required to satisfy the thermal constraint  $T_{\text{return}} \leq 42^\circ\text{C}$  at each CDU branch. The minimum safe flow is computed from the energy balance

as:

$$\dot{m}_{\min} = \max_{j \in \{1,2,3\}} \frac{Q_j}{f_j c_p (T_{\text{limit}} - T_{\text{supply}})} \quad (18)$$

where  $Q_j$  and  $f_j$  denote the heat load and flow fraction for CDU branch  $j$ , respectively.

Figure 4 presents the results of this comparison. Figure 4(a) plots the measured baseline flow against the computed minimum safe flow for all 47,186 operating points. Nearly all points lie above the 1:1 line, confirming systematic over-pumping. The dashed  $1.5\times$  line captures the central tendency of the data. Figure 4(b) shows the histogram of the over-pumping ratio (baseline divided by minimum), with a median of  $1.5\times$ . This indicates that, on average, the facility pumps 50% more coolant than thermally necessary. Because pump power scales as  $P \propto \dot{m}^n$  with  $n \in [2,3]$  under the affinity laws, even a modest flow reduction yields substantial energy savings: a  $1.5\times$  flow reduction corresponds to a  $1.5^3 = 3.4\times$  reduction in pump power under the cubic affinity law.

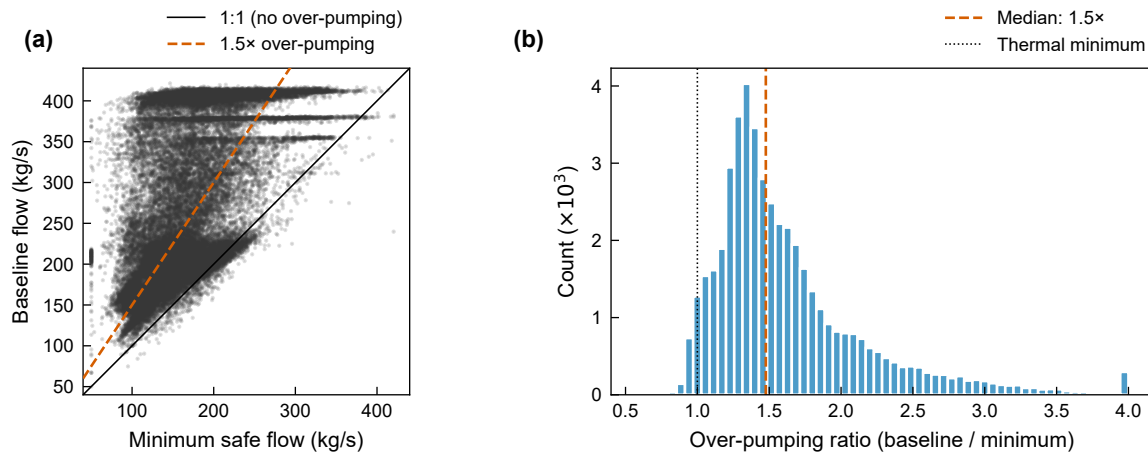


Figure 4: Baseline over-pumping diagnosis: (a) measured baseline flow versus analytically computed minimum safe flow, and (b) distribution of the over-pumping ratio. The median ratio of  $1.5\times$  indicates systematic over-pumping across all operating conditions.

### 3.4 Annual energy comparison across strategies

Four control policies are compared: (1) Baseline (current operations), (2) Strategy A (pump flow optimization only), (3) Strategy B (joint flow and supply temperature setpoint co-optimization with unconstrained ramp rates), and (4) Strategy C (ramp-constrained co-optimization, applying the same objective as Strategy B but enforcing ramp-rate limits

of  $\pm 50$  kg/s per step for flow and  $\pm 1^\circ\text{C}$  per step for  $T_{\text{supply}}$ ). Strategy C follows model predictive control (MPC) principles within the digital twin framework, using the calibrated  $\varepsilon$ -NTU model as the prediction engine while imposing operationally realistic actuator constraints. Table 3 summarizes the annual energy results and Figure 5 provides a visual comparison.

Table 3: Annual cooling energy comparison across optimization strategies (pump exponent  $n = 3$ ). All strategies evaluated using the same optimization framework for consistency.

|   | Baseline         | Strategy A       | Strategy B       | Strategy C        |
|---|------------------|------------------|------------------|-------------------|
| Pump energy (kWh)                             | 488,857          | 118,772          | 180,174          | 193,033           |
| CT fan energy (kWh)                           | 1,324,797        | 1,324,797        | 1,087,613        | 1,116,024         |
| <b>Total (kWh)</b>                            | <b>1,813,654</b> | <b>1,443,569</b> | <b>1,267,787</b> | <b>1,309,057</b>  |
| Pump savings (%)                              | —                | 75.7             | 63.1             | 60.5              |
| CT fan savings (%)                            | —                | 0.0              | 17.9             | 15.8              |
| <b>Total savings (%)</b>                      | —                | <b>20.4</b>      | <b>30.1</b>      | <b>27.8</b>       |
| Mean flow (kg/s)                              | 257              | 163              | 187              | 189               |
| Mean $T_{\text{supply}}$ ( $^\circ\text{C}$ ) | 20.1             | 20.1             | 22.8             | 22.6              |
| Max $T_{\text{return}}$ ( $^\circ\text{C}$ )  | —                | 42.3             | 41.9             | 42.9 <sup>†</sup> |
| Thermal violations <sup>††</sup>              | —                | 2                | 0                | 9                 |

<sup>†</sup>All exceedances occur at the maximum pump capacity (420 kg/s),

indicating a system capacity limit rather than an optimization failure.

<sup>††</sup>Points exceeding the  $42^\circ\text{C}$  optimization constraint; all remain below the  $45^\circ\text{C}$  equipment limit.

A central finding is that cooling tower (CT) fan energy dominates the total cooling energy budget, accounting for 73% of baseline consumption (1,325 MWh out of 1,814 MWh). This 2.7:1 ratio between CT fan and pump energy has important strategic implications. Strategy A, which optimizes only pump flow, achieves a 75.7% reduction in pump energy but leaves the larger CT component untouched, yielding 20.4% total savings. Strategy B introduces supply temperature setpoint reset as an additional decision variable, enabling the optimizer to raise  $T_{\text{supply}}$  by an average of  $2.7^\circ\text{C}$ . This reduces the CT fan workload by 17.9% while accepting slightly higher pump energy than Strategy A (63.1% vs. 75.7%

pump savings). The net result is a 30.1% total savings for Strategy B, representing a 48% improvement over the flow-only approach. Strategy C, which enforces operationally realistic ramp-rate constraints, achieves 27.8% total savings, recovering 92.4% of the unconstrained theoretical bound established by Strategy B.

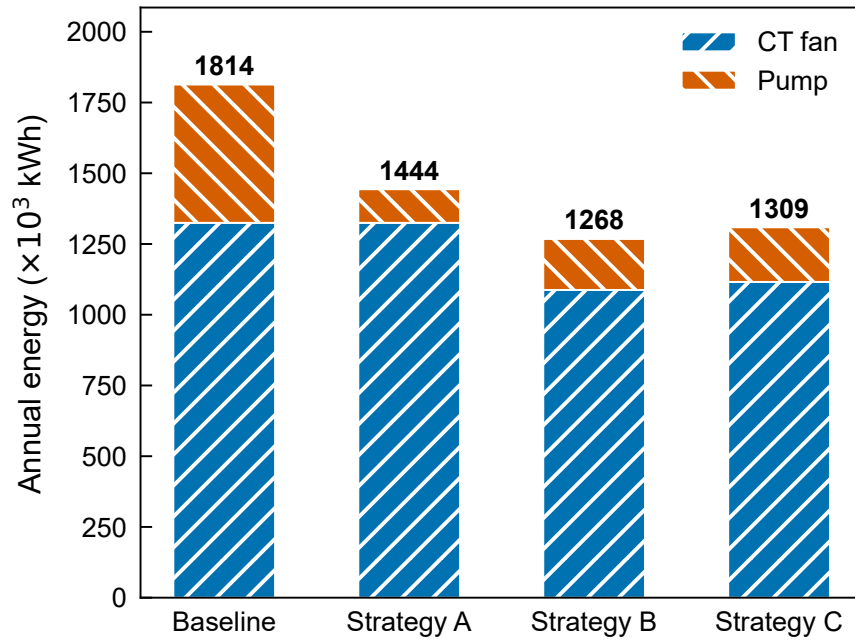


Figure 5: Annual cooling energy breakdown by component (pump vs. CT fan) for each optimization strategy. Stacked bars show the relative contributions; total values are annotated in thousands of kWh.

### 3.5 Monthly and seasonal energy profiles

Figure 6 presents the monthly total cooling energy for all four strategies. The savings are not uniformly distributed across the year. Winter months (January through March) exhibit savings of approximately 15–20%, constrained by the already-low supply temperatures that limit room for setpoint adjustment. Summer months (May through September) realize the largest absolute savings, where the optimizer simultaneously reduces excess flow and raises  $T_{\text{supply}}$  to avoid unnecessary subcooling by the cooling tower. The peak monthly saving of 33% occurs in July, when the baseline cooling load is highest.

Figure 7 provides a compact overview of the savings across all months and strategies. The color-coded heatmap reveals a clear seasonal structure: Strategy A contributes mini-

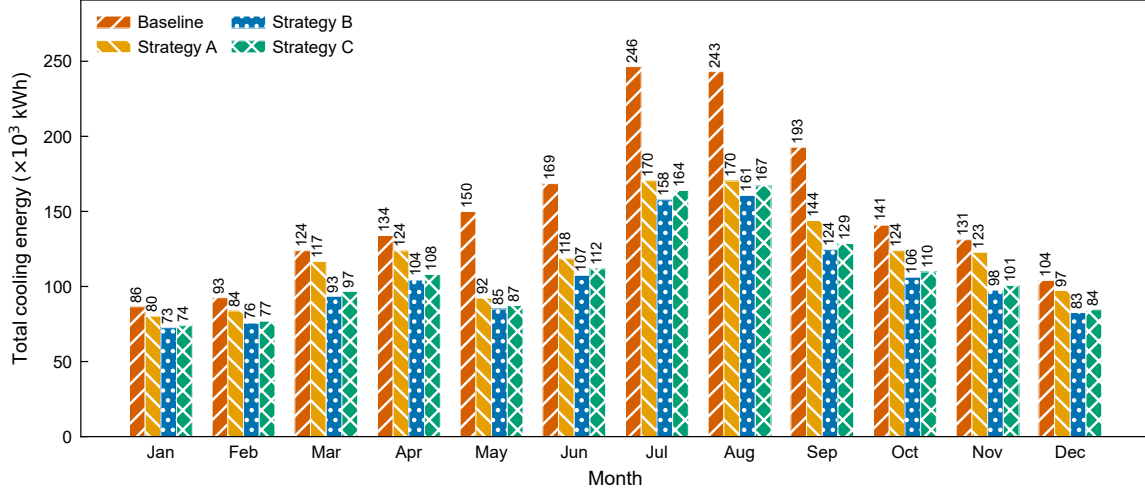


Figure 6: Monthly total cooling energy (pump + CT fan) across four strategies. Strategy C achieves the largest savings during high-load summer months, with a peak of 33% reduction in July.

mally during winter (6–10%) but achieves 25–37% during summer, when the baseline flow is most inflated relative to thermal need. Strategies B and C consistently outperform Strategy A across all months, with the largest absolute advantage during the shoulder seasons (March through April, October through November) where setpoint reset remains effective even when pump savings are modest. Notably, the gap between Strategy B and Strategy C is smallest during summer (1–3%), indicating that the ramp-rate constraints impose the least penalty precisely when savings are highest.

Table 4 quantifies the seasonal breakdown. The summer period (June through August) accounts for 43% of total annual savings under Strategy C despite spanning only 25% of the calendar year. The implementability cost of ramp-rate constraints, defined as the gap between Strategies B and C, varies from 1.5% in winter to 2.6% in summer. The relative cost is largest during winter, when smaller absolute savings amplify the impact of constraint-induced lag.

### 3.6 Supply temperature setpoint mechanism

The mechanism by which supply temperature co-optimization achieves additional savings is illustrated in Figure 8. Figure 8(a) shows the distribution of  $\Delta T_{\text{supply}}$  (optimized minus

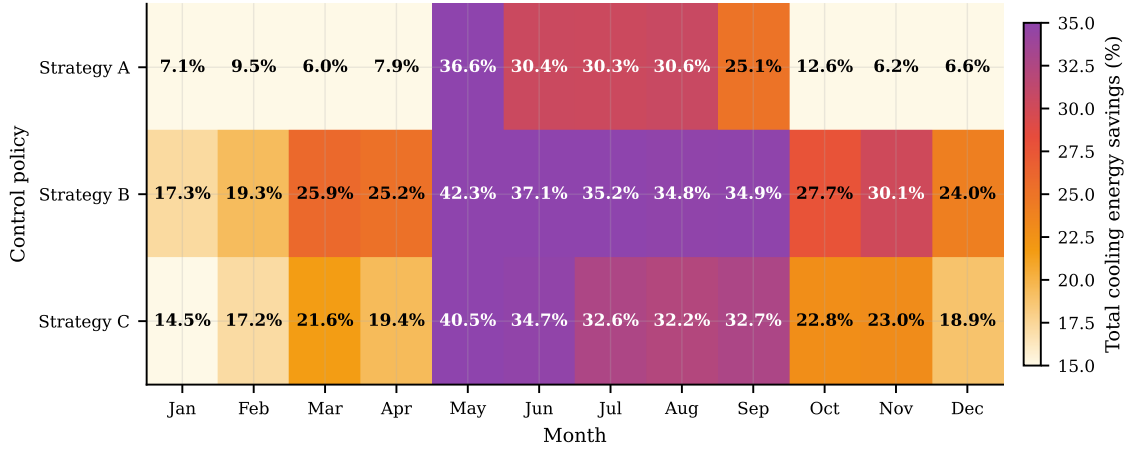


Figure 7: Monthly total cooling energy savings (%) by control policy. Color intensity indicates magnitude. Co-optimization strategies (B and C) outperform flow-only optimization (A) across all months, with the advantage most pronounced during shoulder and winter seasons.

baseline) across all operating points. The optimizer raises  $T_{\text{supply}}$  by a mean of  $+2.7^{\circ}\text{C}$  in 97.9% of timesteps, while lowering it in only 2.0% of cases (typically during transient high-load events). Figure 8(b) compares the monthly mean  $T_{\text{supply}}$  for Baseline, Strategy B, and Strategy C. The optimized strategies consistently maintain a higher setpoint than the baseline, with the gap widening in summer when the trade-off between pump and CT energy is most consequential. During winter, the baseline supply temperature is already near the cooling water temperature, leaving limited room for further adjustment; Strategies B and C converge near the baseline values.

The physical interpretation is that the existing control system overcools the supply water below what is thermally necessary, forcing the cooling tower to work harder to produce unnecessarily cold cooling water. By raising  $T_{\text{supply}}$ , the optimizer accepts a warmer supply stream, which reduces the CT approach temperature and corresponding fan power, at the cost of requiring slightly more pump flow to maintain the return temperature below  $42^{\circ}\text{C}$ . The net energy trade-off favors the raised setpoint in nearly all conditions.

Table 4: Seasonal cooling energy comparison and total savings by strategy.

|                  | Energy (MWh) |              |              |              | Savings (%) |             |             |
|------------------|--------------|--------------|--------------|--------------|-------------|-------------|-------------|
|                  | Baseline     | A            | B            | C            | A           | B           | C           |
| Winter (Dec–Feb) | 280          | 259          | 229          | 233          | 7.6         | 18.5        | 17.0        |
| Spring (Mar–May) | 407          | 333          | 284          | 293          | 18.1        | 30.3        | 28.0        |
| Summer (Jun–Aug) | 659          | 458          | 425          | 442          | 30.5        | 35.5        | 33.0        |
| Fall (Sep–Nov)   | 467          | 393          | 331          | 341          | 15.9        | 29.2        | 26.9        |
| <b>Annual</b>    | <b>1,814</b> | <b>1,444</b> | <b>1,268</b> | <b>1,309</b> | <b>20.4</b> | <b>30.1</b> | <b>27.8</b> |

### 3.7 Operating envelope shift

Figure 9 presents the joint distribution of flow rate and supply temperature for Baseline, Strategy B, and Strategy C, visualized through kernel density contours overlaid on the raw operating points. Under baseline operations (Figure 9(a)), the facility occupies a broad operating envelope centered at 257 kg/s mean flow and 20.1°C mean supply temperature, with a characteristic bimodal structure reflecting the seasonal flow step change observed in Figure 3.

Strategy B (Figure 9(b)) shifts the operating envelope toward lower flow rates ( $\mu = 187$  kg/s) and higher supply temperatures ( $\mu = 22.8^\circ\text{C}$ ), compressing the flow distribution and eliminating the high-flow summer mode. Strategy C (Figure 9(c)) exhibits a nearly identical centroid ( $\mu = 189$  kg/s, 22.6°C) but with a slightly broader distribution, reflecting the smoothing effect of ramp-rate constraints that prevent the optimizer from reaching the instantaneous setpoint at every timestep. The similarity between the Strategy B and Strategy C envelopes confirms that the ramp constraints primarily affect transition dynamics rather than the steady-state operating target.

### 3.8 Strategy C dynamic behavior under constraints

Figure 10 presents a representative summer week (168 hours in July), comparing the dynamic trajectories of Baseline, Strategy B, and Strategy C across four variables. Figure 10(a) shows the flow rate: the baseline operates near 400 kg/s with abrupt step changes,

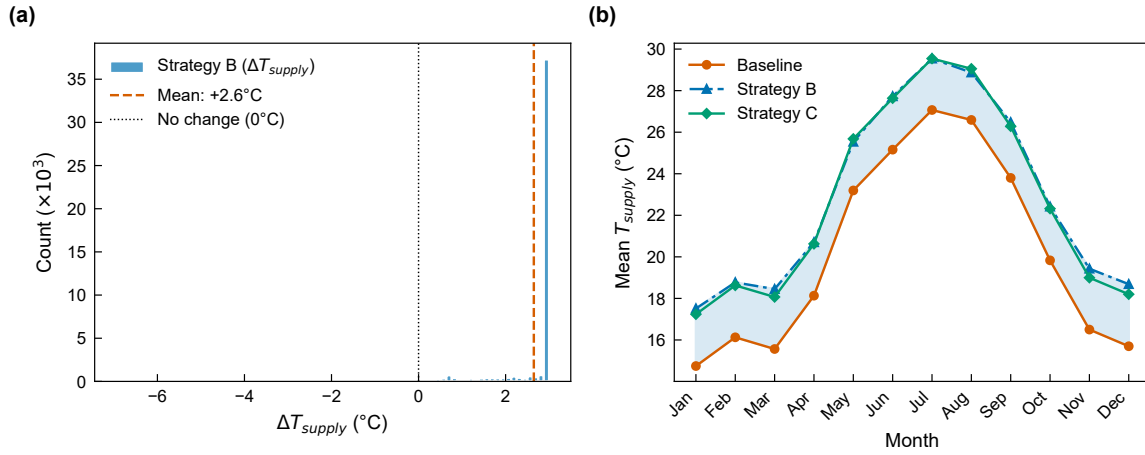


Figure 8: Supply temperature setpoint reset mechanism: (a) distribution of  $\Delta T_{supply}$  showing a mean increase of +2.7°C, and (b) monthly mean  $T_{supply}$  comparing Baseline, Strategy B, and Strategy C. The shaded region highlights the additional headroom exploited by optimization.

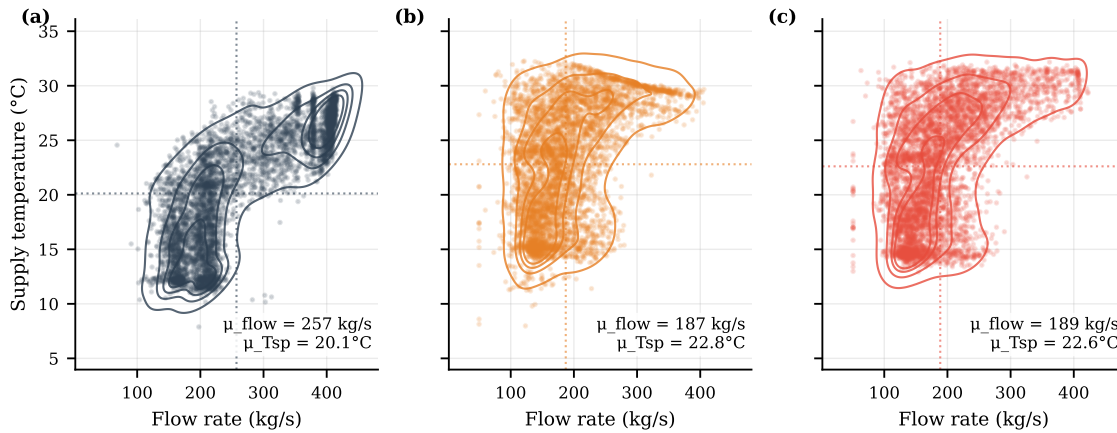


Figure 9: Joint distribution of flow rate and supply temperature for (a) Baseline, (b) Strategy B, and (c) Strategy C. Contour lines show kernel density estimates; dotted lines indicate mean values. Co-optimization shifts the operating envelope toward lower flow and higher supply temperature, while Strategy C closely tracks the Strategy B centroid with modestly broader spread due to ramp-rate constraints.

while both optimized strategies modulate flow between 150 and 400 kg/s in response to load variations. The Strategy C trajectory is smoother than Strategy B, as the ramp-rate constraints prevent large instantaneous jumps. Figure 10(b) shows  $T_{\text{supply}}$ : Strategy C maintains a consistently higher setpoint (28–32°C) compared to the baseline (24–28°C), reflecting the setpoint reset mechanism. Figure 10(c) demonstrates the resulting total power reduction, with Strategy C achieving 30–50% lower instantaneous power during most of the week. Figure 10(d) confirms that Strategy C operates near the 42°C return temperature constraint throughout, with the few exceedances occurring exclusively at the maximum pump capacity (420 kg/s), where the system has exhausted its flow control authority. All operating points remain below the 45°C equipment limit.

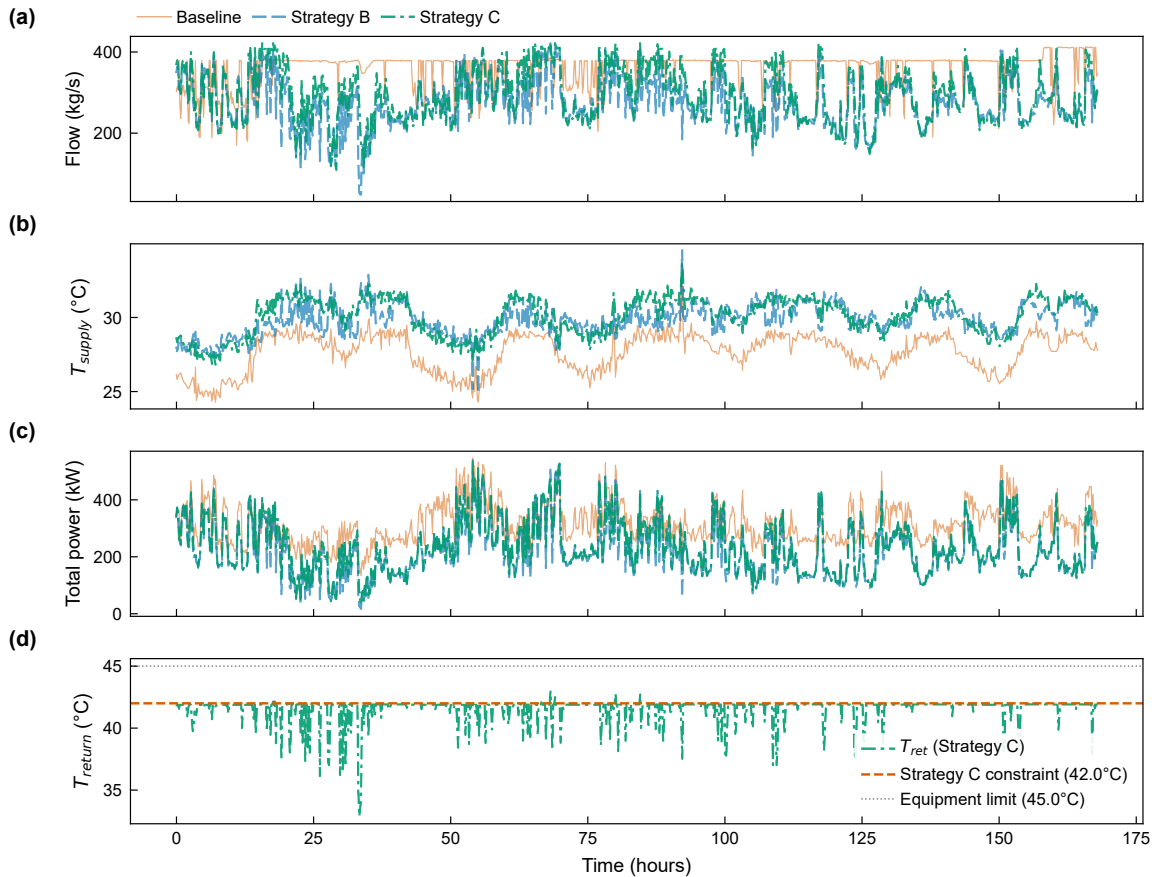


Figure 10: Representative summer week (July) comparing Baseline, Strategy B, and Strategy C: (a) flow rate, (b) supply temperature setpoint, (c) total cooling power, and (d) return temperature with constraint thresholds. Strategy C maintains near-complete constraint compliance while achieving significant power reduction.

### 3.9 Ramp-rate compliance

A key practical concern for real-world deployment is whether the optimization commands can be tracked by physical actuators without inducing water hammer, thermal shock, or control instability. Figure 11 directly addresses this by plotting the absolute step-to-step change in flow rate (Figure 11(a)) and  $T_{\text{supply}}$  setpoint (Figure 11(b)) for both the unconstrained Strategy B and the ramp-constrained Strategy C.

Strategy B produces flow rate changes up to 189 kg/s per 10-minute step and temperature changes up to 4.4°C per step, frequently violating both the  $\pm 50$  kg/s and  $\pm 1^\circ\text{C}$  limits that represent conservative actuator and process constraints. These ramp-rate limits are informed by typical variable-frequency drive slew rates and thermal inertia considerations for large-scale chilled and hot water distribution systems (ASHRAE, 2020). Strategy C, by contrast, respects both ramp-rate limits by construction. Temperature setpoint changes under Strategy C are strictly bounded below  $\pm 1^\circ\text{C}$ , and flow rate changes remain within the  $\pm 50$  kg/s envelope throughout normal operation. This constraint satisfaction comes at a modest cost: Strategy C achieves 27.8% total savings versus 30.1% for Strategy B, retaining 92.4% of the unconstrained theoretical bound.

### 3.10 Pump power duration curves

Figure 12 presents the annual pump power duration curves for all four strategies, providing an alternative perspective on the savings distribution across operating hours. The baseline curve shows pump power exceeding 100 kW for approximately 55% of the year, with a peak near 200 kW. All three optimized strategies shift the curve downward substantially. Strategy A (flow only) achieves the largest pump power reduction, since it minimizes flow without regard for CT energy. Strategies B and C maintain slightly higher pump power levels (as they trade pump energy for CT savings), but the overall shift relative to the baseline remains large. Notably, the Strategy C curve lies slightly above Strategy B in the 20–60% exceedance range, reflecting the ramp-rate constraints that prevent Strategy C from reaching the instantaneous optimum at every timestep.

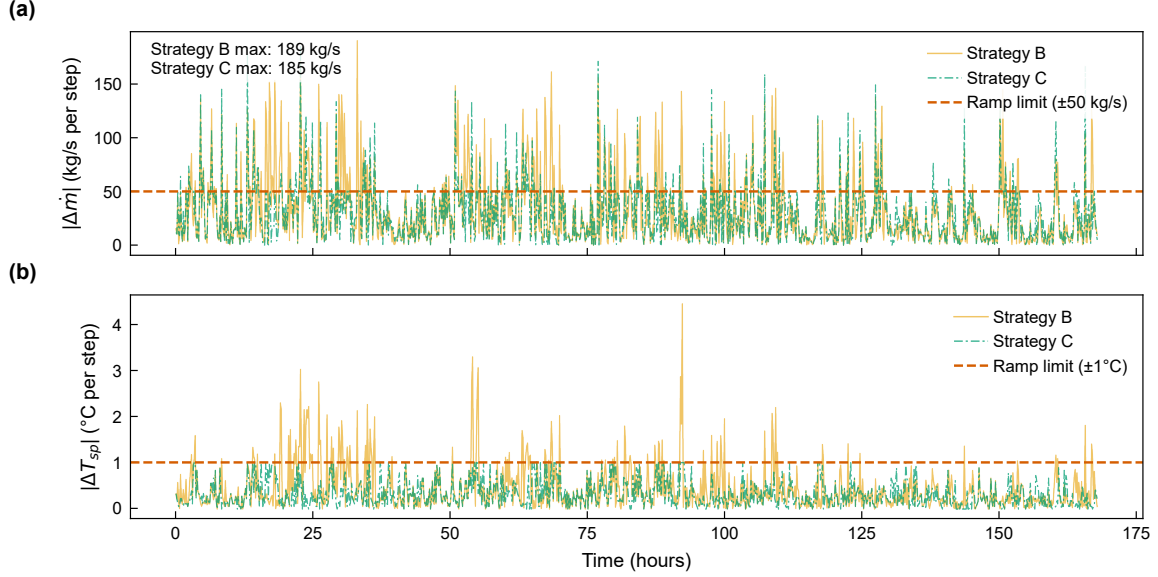


Figure 11: Step-to-step ramp-rate comparison between unconstrained Strategy B and ramp-constrained Strategy C during a summer week: (a) flow rate changes with  $\pm 50$  kg/s limit, and (b)  $T_{\text{supply}}$  setpoint changes with  $\pm 1^\circ\text{C}$  limit. Strategy C respects both operational constraints while Strategy B frequently violates them.

### 3.11 Sensitivity to pump curve exponent

The pump power model  $P_{\text{pump}} = P_{\text{pump,nom}}(\dot{m}/\dot{m}_{\text{nom}})^n$  Equation (4) depends on the exponent  $n$ , which ranges from  $n = 2$  (conservative estimate with residual static head) to  $n = 3$  (standard affinity law for fully turbulent flow). Because the exact Frontier pump curves are not publicly available, we evaluate all strategies across three representative exponents. Table 5 and Figure 13 present these results.

Table 5: Total cooling energy savings (%) across pump curve exponents and strategies.

| Pump exponent                        | Strategy A | Strategy B | Strategy C |
|--------------------------------------|------------|------------|------------|
| $P \propto \dot{m}^2$ (conservative) | 10.9       | 23.3       | 21.3       |
| $P \propto \dot{m}^{2.5}$ (typical)  | 15.2       | 26.3       | 24.2       |
| $P \propto \dot{m}^3$ (affinity law) | 20.4       | 30.1       | 27.8       |

The sensitivity analysis reveals two important insights. First, the total savings increase monotonically with the pump exponent across all strategies, as expected from the nonlinear

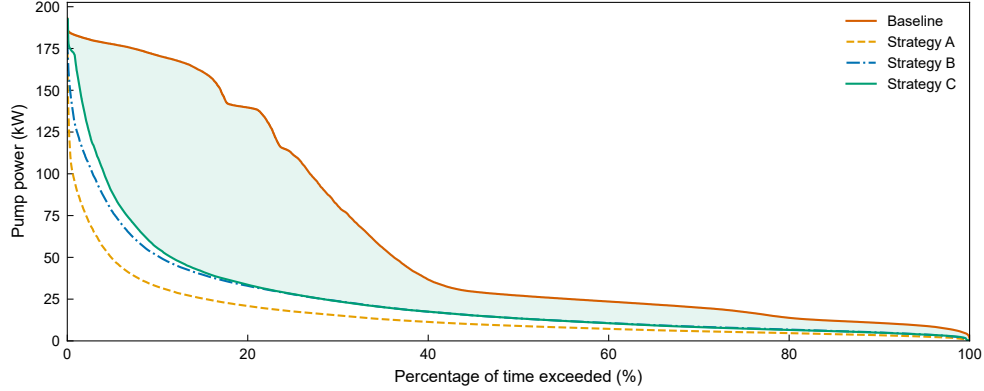


Figure 12: Annual pump power duration curves showing the distribution of pump power across all operating hours. All optimization strategies substantially reduce pump power relative to the baseline, with the greatest reductions during high-load summer operation.

relationship between flow and power. Under the most conservative assumption ( $n = 2$ ), Strategy C still achieves 21.3% total savings; under the standard affinity law ( $n = 3$ ), the savings reach 27.8%. This 21–28% range provides a robust bound on the expected benefits. Second, the relative advantage of co-optimization (Strategies B and C) over flow-only optimization (Strategy A) is most pronounced at lower pump exponents. At  $n = 2$ , Strategy C nearly doubles the savings of Strategy A (21.3% vs. 10.9%), because when pump power is less sensitive to flow, the CT fan savings from setpoint reset become the dominant contributor. At  $n = 3$ , Strategy C achieves a 36% relative improvement over Strategy A (27.8% vs. 20.4%). This demonstrates that supply temperature co-optimization is valuable across the full range of plausible pump characteristics.

## 4 Discussion

### 4.1 System-level perspective on cooling system optimization

A primary contribution of this work is the demonstration that optimizing pump flow alone captures only a fraction of the available cooling energy savings. The finding that CT fan energy constitutes 73% of the total cooling energy budget fundamentally shifts the optimization landscape. While the pump affinity law ( $P \propto \dot{m}^3$ ) makes flow reduction an attractive target in isolation, the system-level optimum lies in coordinating pump flow and

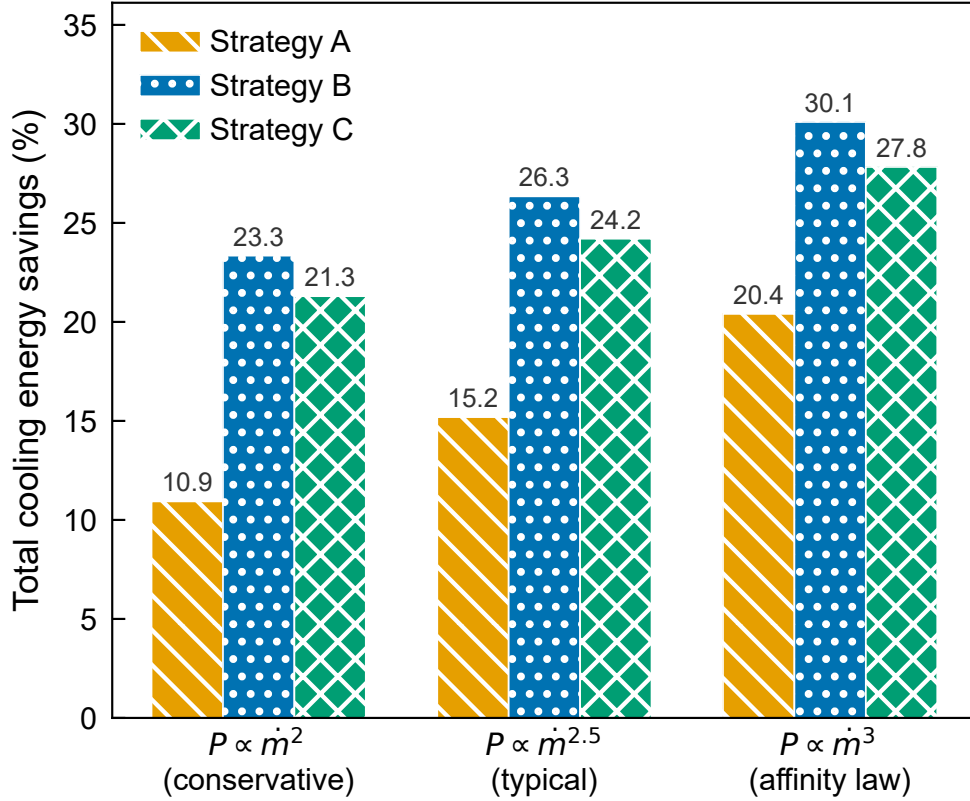


Figure 13: Sensitivity of total cooling energy savings to pump curve exponent for all three optimization strategies. Co-optimization (Strategies B and C) consistently outperforms flow-only optimization across all exponents.

supply temperature setpoint to minimize the combined pump and CT fan consumption. This coordination produces a counterintuitive outcome: the co-optimized Strategy B uses *more* pump energy than the flow-only Strategy A (180,174 vs. 118,772 kWh), yet achieves greater total savings (30.1% vs. 20.4%) by reducing the dominant CT fan component.

This finding aligns with the broader principle that component-level optimization can be suboptimal when interdependencies exist between subsystems. In data center cooling, lowering the supply temperature requires the cooling tower to produce colder water, which demands more fan energy. The digital twin captures these interdependencies through the coupled  $\varepsilon$ -NTU heat exchanger model and the cooling tower performance curves, enabling the optimizer to navigate the pump-versus-CT trade-off at each operating point. The operating envelope analysis (Figure 9) further illustrates this rebalancing: the shift from the baseline centroid (257 kg/s, 20.1°C) to the co-optimized centroid (187–189 kg/s, 22.6–

22.8°C) reflects a deliberate reallocation of energy between the two subsystems rather than simple minimization of either one.

## 4.2 *Practical implementability of the ramp-constrained strategy*

Strategy C addresses a gap often observed in optimization studies that report unconstrained theoretical savings without considering actuator limitations. The  $\pm 50$  kg/s flow rate limit and  $\pm 1^\circ\text{C}$  setpoint change limit per 10-minute step represent conservative bounds informed by typical variable-frequency drive slew rates and thermal inertia considerations for large-scale cooling systems (ASHRAE, 2020). Strategy C recovers 92.4% of the unconstrained savings established by Strategy B (27.8% vs. 30.1%) while producing smooth, actuator-friendly control trajectories. The 2.3% reduction from the theoretical bound is the cost of implementability, a modest penalty for a strategy that can be deployed on real hardware without risking water hammer, thermal shock, or control oscillations.

The seasonal analysis (Table 4) provides additional nuance: the implementability gap ranges from 1.5% in winter to 2.6% in summer in absolute terms, though the relative impact is proportionally larger during winter when the total savings base is smaller. This pattern arises because winter conditions offer limited  $T_{\text{supply}}$  headroom, and the ramp constraints slow convergence to the optimal setpoint during brief warm-weather excursions. A seasonally adaptive ramp-rate policy could further narrow this gap, though such refinement is left for future work.

The nine thermal exceedances observed under Strategy C (Table 3) all occur at the maximum pump capacity of 420 kg/s during extreme summer load peaks, where the system has exhausted its flow control authority. The maximum return temperature of  $42.9^\circ\text{C}$  remains well below the  $45^\circ\text{C}$  equipment limit, and the exceedances represent 0.02% of all operating points. These capacity-limited events are inherent to the system design rather than a deficiency of the optimization strategy, and the  $3^\circ\text{C}$  safety margin between the optimization constraint ( $42^\circ\text{C}$ ) and the equipment limit ( $45^\circ\text{C}$ ) provides adequate defense-in-depth against such excursions.

### **4.3 Robustness across pump curve uncertainty**

The 21–28% savings range across pump exponents (Table 5) provides confidence that the proposed approach is robust to uncertainty in the pump power model. This is practically significant because detailed pump curves for installed equipment are often unavailable to researchers and operators. Even under the most conservative assumption ( $P \propto \dot{m}^2$ ), Strategy C achieves over 21% total cooling energy savings, representing approximately 380 MWh of annual reduction for the Frontier facility. Under the typical assumption ( $P \propto \dot{m}^{2.5}$ ), the savings reach 24.2%, corresponding to approximately 435 MWh annually. At utility rates typical for the Oak Ridge area, these savings translate to an estimated annual cost reduction on the order of \$30,000–\$50,000, with the additional benefit of reduced carbon emissions proportional to the local grid emission factor.

### **4.4 Scalability and generalizability**

The methodology is applicable to other liquid-cooled data centers that employ external heat exchangers and cooling towers, provided that sufficient operational data are available for digital twin calibration. The Modelica-based modeling framework enables component substitution (e.g., replacing the counterflow heat exchanger with a crossflow configuration) without modifying the optimization algorithm. The  $\varepsilon$ -NTU analytical model used within the Strategy C optimizer is computationally lightweight, solving each 10-minute optimization in under 10 milliseconds on a standard workstation. This computational efficiency makes the approach suitable for deployment as an online supervisory controller with a 10-minute update cycle.

### **4.5 Limitations and future work**

Several limitations should be noted. First, the cooling tower fan model employs a simplified power-approach relationship calibrated to DOE performance curves, rather than a manufacturer-specific model for the Frontier installation. The CT fan savings should therefore be interpreted as directionally correct rather than exact. Second, the optimization assumes that the supply temperature setpoint can be independently adjusted from the cooling tower operation, which may require control system modifications at the facility

level. Third, the current study uses a static (point-by-point) optimization with retrospective ramp-rate enforcement; a full receding-horizon MPC formulation with multi-step look-ahead capability could further improve performance during rapid load transients. Finally, the digital twin validation (ASHRAE Guideline 14 compliant, as reported in Section 3.1) was performed using a steady-state energy balance with an adopted  $c_p$  that differs by 6% from the dataset’s internal conversion constant (Section 2.3.2); transient validation during load ramps and independent calorimetric measurement of  $c_p$  would strengthen confidence in the absolute predictions.

Future work will focus on three extensions: (1) integration of weather forecasting to enable predictive setpoint scheduling, (2) experimental validation through a pilot deployment on a subset of CDU branches, and (3) extension of the framework to facilities with chilled-water systems, where the optimization trade-offs between chiller and cooling tower energy present analogous coupling effects.

## 5 Conclusion

This paper developed a digital twin for the Frontier exascale supercomputer’s liquid cooling system and established three progressively complex optimization strategies through one full year of operational data. The study produced four principal findings.

First, the dominant source of cooling energy consumption is not where conventional intuition suggests. Cooling tower fan energy accounts for 73% of the total cooling energy budget at Frontier, while pump energy accounts for only 27%. This asymmetry means that optimizing pump flow in isolation, despite the attractive cubic relationship between flow and pump power, captures only a fraction of the available savings. Strategy A (flow-only optimization) achieves 20.4% total savings, but Strategy B (co-optimization of flow and supply temperature) reaches 30.1% by reducing the cooling tower workload through a modest mean supply temperature increase of 2.7°C. The co-optimized strategy uses *more* pump energy than the flow-only strategy, yet achieves greater total savings. This counter-intuitive result underscores the importance of system-level thinking over component-level optimization, a principle with broad applicability across coupled thermal systems.

Second, the gap between theoretical optimality and practical implementability is surpris-

ingly small for this system. Strategy C, which enforces ramp-rate constraints of  $\pm 50$  kg/s per step and  $\pm 1^\circ\text{C}$  per step on the co-optimized solution, recovers 92.4% of the unconstrained savings (27.8% vs. 30.1%). The implementability cost of 2.3% is modest in absolute terms and does not vary substantially across seasons (1.5–2.6%). This finding suggests that for large-scale liquid cooling systems with smooth thermal dynamics, practitioners can pursue near-optimal energy performance without sacrificing the actuator smoothness and operational predictability that real-world deployment demands.

Third, the proposed methodology is robust to parametric uncertainty. Across the full range of plausible pump power exponents ( $n = 2$  to  $n = 3$ ), Strategy C achieves 21–28% total cooling energy savings. Even under the most conservative assumption ( $P \propto \dot{m}^2$ ), the savings exceed 21%, providing a reliable lower bound for facility managers who may lack detailed pump curve data for installed equipment.

Fourth, the digital twin validation demonstrates that a physics-based model with a single calibration parameter (glycol mass fraction) can predict per-subloop return temperatures to within 1.96–2.67% CV-RMSE against ASHRAE Guideline 14 criteria, using the Modelica Buildings Library as the modeling foundation. This confirms the viability of equation-based digital twins as optimization testbeds for HPC cooling infrastructure, where the physical transparency of the model is essential for operator trust and regulatory acceptance.

From a methodological standpoint, this work introduces two concepts that extend beyond the specific application. The *implementability gap* metric provides a formal, reproducible measure of the energy penalty imposed by practical constraints on theoretically optimal control. The *layered optimization* framework, which progresses from single-variable to multi-variable to constrained formulations, offers a systematic protocol for decomposing the sources of energy savings and evaluating the cost of operational realism. These concepts are applicable to any coupled thermal system where the gap between simulation-derived optima and deployable control strategies is a concern.

The computational efficiency of the SLSQP-based optimizer (under 10 ms per timestep) makes online supervisory control feasible within a 10-minute update cycle, and the Modelica framework enables straightforward adaptation to alternative cooling architectures through component substitution. As HPC facilities continue to scale toward multi-exascale power envelopes, the gap between theoretical and implementable efficiency will only widen unless

it is systematically measured. The tools introduced here provide a foundation for that measurement.

## 6 Acknowledgment

The authors acknowledge the generous support from the University of Michigan Office of the Vice President.

## 7 Data and code availability

The data and computer code used in this study are not yet publicly available, but will be made publicly available at the time of paper acceptance.

## References

- Afram, A. and F. Janabi-Sharifi (2014). Review of modeling methods for HVAC systems. *Applied Thermal Engineering* 67(1–2), 507–519.
- ASHRAE (2014). ASHRAE Guideline 14-2014: Measurement of energy, demand, and water savings. Technical report, American Society of Heating, Refrigerating and Air-Conditioning Engineers, Atlanta, GA.
- ASHRAE (2020). *ASHRAE Handbook: HVAC Systems and Equipment*. Atlanta, GA: American Society of Heating, Refrigerating and Air-Conditioning Engineers.
- Athavale, J., C. Bash, W. Brewer, et al. (2024). Digital twins for data centers. *Computer* 57(10), 151–158.
- Brewer, W., M. Maiterth, V. Kumar, et al. (2024). A digital twin framework for liquid-cooled supercomputers as demonstrated at exascale. In *SC '24: Proceedings of the International Conference for High Performance Computing, Networking, Storage and Analysis*, pp. 1–18.
- Chen, B., Z. Cai, and M. Bergés (2020). Gnu-RL: A practical and scalable reinforcement learning solution for building HVAC control using a differentiable MPC policy. *Frontiers in Built Environment* 6, 562239.
- de Wilde, P. (2014). The gap between predicted and measured energy performance of buildings: A framework for investigation. *Automation in Construction* 41, 40–49.
- Ebrahimi, K., G. F. Jones, and A. S. Fleischer (2014). A review of data center cooling technology, operating conditions and the corresponding low-grade waste heat recovery opportunities. *Renewable and Sustainable Energy Reviews* 31, 622–638.

- Evans, R. and J. Gao (2016, July). DeepMind AI reduces Google data centre cooling bill by 40%. DeepMind Blog.
- Fan, C., K. Hinkelman, Y. Fu, et al. (2021). Open-source Modelica models for the control performance simulation of chiller plants with water-side economizer. *Applied Energy* 299, 117337.
- Fu, Y., W. Zuo, M. Wetter, J. W. VanGilder, X. Han, and D. Plamondon (2019). Equation-based object-oriented modeling and simulation for data center cooling: A case study. *Energy and Buildings* 186, 108–125.
- Fu, Y., W. Zuo, M. Wetter, J. W. VanGilder, and P. Yang (2019). Equation-based object-oriented modeling and simulation of data center cooling systems. *Energy and Buildings* 198, 503–519.
- Grahovac, M., P. Ehrlich, J. Hu, and M. Wetter (2023). Model-based data center cooling controls comparative co-design. *Science and Technology for the Built Environment* 30(4), 394–414.
- Grant, D., L. Bortot, C. DePrater, D. Martinez, R. Grant, and N. Bates (2026). Providing thermal stability for an exascale supercomputer: A case study of Frontier’s cooling system. In *Proceedings of Supercomputing Asia and ICHPC*, pp. 69–78.
- Greenwood, S., V. Kumar, and W. Brewer (2024). Thermo-fluid modeling framework for supercomputing digital twins: Part 2, automated cooling models. In *Proceedings of the American Modelica Conference*.
- Grieves, M. and J. Vickers (2017). Digital twin: Mitigating unpredictable, undesirable emergent behavior in complex systems. In *Transdisciplinary Perspectives on Complex Systems*, pp. 85–113. Springer.
- Hashmi, M. U., D. Van Hertem, A. van der Meer, and A. Keane (2024). Linear energy storage and flexibility model with ramp rate, ramping, deadline and capacity constraints. *arXiv preprint arXiv:2409.08084*.
- Hinkelman, K., J. Wang, W. Zuo, et al. (2022). Modelica-based modeling and simulation of district cooling systems: A case study. *Applied Energy* 311, 118654.
- Incropera, F. P., D. P. DeWitt, T. L. Bergman, and A. S. Lavine (2007). *Fundamentals of Heat and Mass Transfer* (6th ed.). Hoboken, NJ: John Wiley & Sons.
- International Energy Agency (2025). Energy and AI. Technical report, IEA, Paris. IEA Special Report.
- Jadhav, S. and Z. Liu (2026). Machine learning guided cooling optimization for data centers. *arXiv preprint arXiv:2601.02275*.
- Karimi, A. M., M. Maiterth, W. Shin, et al. (2024). Exploring the frontiers of energy efficiency using power management at system scale. In *SC '24 Workshops*, pp. 1835–1844.

- Knapp, G. L., T. Mukherjee, J. S. Zuback, H. L. Wei, T. A. Palmer, A. De, and T. DebRoy (2020). Toward the digital twin of additive manufacturing. *IISE Transactions* 52(11), 1204–1217.
- Kraft, D. (1988). A software package for sequential quadratic programming. Technical Report DFVLR-FB 88-28, DFVLR, Köln.
- Kumar, V., S. Greenwood, W. Brewer, D. Grant, N. Parkison, and W. Williams (2024). Thermo-fluid modeling framework for supercomputing digital twins: Part 1, demonstration at exascale. In *Proceedings of the American Modelica Conference*.
- Lazic, N., C. Boutilier, T. Lu, et al. (2018). Data center cooling using model-predictive control. In *Advances in Neural Information Processing Systems (NeurIPS)*, pp. 3814–3823.
- Li, Y., Y. Wen, D. Tao, and K. Guan (2020). Transforming cooling optimization for green data center via deep reinforcement learning. *IEEE Transactions on Cybernetics* 50(5), 2002–2013.
- Ma, Y., F. Borrelli, B. Hancey, et al. (2012). Model predictive control for the operation of building cooling systems. *IEEE Transactions on Control Systems Technology* 20(3), 796–803.
- Maasoumy, M., M. Razmara, M. Shahbakhti, and A. Sangiovanni-Vincentelli (2014). Handling model uncertainty in model predictive control for energy efficient buildings. *Energy and Buildings* 77, 377–392.
- Masanet, E., A. Shehabi, N. Lei, S. Smith, and J. Koomey (2020). Recalibrating global data center energy-use estimates. *Science* 367(6481), 984–986.
- Melinder, Å. (2010). *Properties of Secondary Working Fluids (Secondary Refrigerants or Coolants, Heat Transfer Fluids) for Indirect Systems*. Paris: International Institute of Refrigeration (IIR/IIF).
- Oldewurtel, F., A. Parisio, C. N. Jones, et al. (2012). Use of model predictive control and weather forecasts for energy efficient building climate control. *Energy and Buildings* 45, 15–27.
- Salvato, E., G. Fenu, E. Medvet, and F. A. Pellegrino (2021). Crossing the reality gap: A survey on sim-to-real transferability of robot controllers in reinforcement learning. *IEEE Access* 9, 153171–153187.
- Sarkar, S., A. Naug, A. Guillen, et al. (2024). Sustainability of data center digital twins with reinforcement learning. In *Proceedings of the AAAI Conference on Artificial Intelligence*, Volume 38, pp. 22322–22330.
- Shehabi, A., S. J. Smith, A. Hubbard, et al. (2024). 2024 United States data center energy usage report. Technical Report LBNL-2001637, Lawrence Berkeley National Laboratory.
- Sun, J., Z. Gao, D. Grant, K. Nawaz, P. Wang, C.-M. Yang, P. Boudreaux, S. Kowalski, and S. Huff (2024). Energy dataset of Frontier supercomputer for waste heat recovery. *Scientific Data* 11(1), 1077.

- Tan, Y. and A. Matta (2024). The digital twin synchronization problem: Framework, formulations, and analysis. *IISE Transactions* 56(6), 652–665.
- Tao, F., H. Zhang, A. Liu, and A. Y. C. Nee (2019). Digital twin in industry: State-of-the-art. *IEEE Transactions on Industrial Informatics* 15(4), 2405–2415.
- Uptime Institute (2024). Global data center survey results 2024. Technical report, Uptime Institute.
- Van Dronkelaar, C., M. Dowson, E. Burman, C. Spataru, and D. Mumovic (2016). A review of the energy performance gap and its underlying causes in non-domestic buildings. *Frontiers in Mechanical Engineering* 1, 17.
- Wang, P., S. Kowalski, Z. Gao, et al. (2024). District heating utilizing waste heat of a data center: High-temperature heat pumps. *Energy and Buildings* 315, 114327.
- Wetter, M., K. Benne, H. Tummescheit, and C. Winther (2024). Spawn: coupling Modelica Buildings Library and EnergyPlus. *Journal of Building Performance Simulation* 17(2), 274–292.
- Wetter, M., W. Zuo, T. S. Noudui, and X. Pang (2014). Modelica Buildings library. *Journal of Building Performance Simulation* 7(4), 253–270.
- Zhan, X., X. Zhu, P. Cheng, et al. (2025). Data center cooling system optimization using offline reinforcement learning. *arXiv preprint arXiv:2501.15085*.
- Zhang, Q., C. Tang, T. Bai, et al. (2021). A survey on data center cooling systems: Technology, power consumption modeling and control strategy optimization. *Journal of Systems Architecture* 119, 102253.
- Zhao, W., J. P. n. Queraltá, and T. Westerlund (2020). Sim-to-real transfer in deep reinforcement learning for robotics: A survey. In *IEEE Symposium Series on Computational Intelligence (SSCI)*, pp. 737–744.
- Zhu, H. and B. Lin (2024). Digital twin-driven energy consumption management of integrated heat pipe cooling system for a data center. *Applied Energy* 373, 123840.